The Astrophysical Journal, 966:87 (32pp), 2024 May 1 https://doi.org/10.3847/1538-4357/ad2f2a

The Physical Properties of Low-redshift FeLoBAL Quasars. IV. Optical–Near-IR Spectral Energy Distributions and Near-IR Variability Properties

Karen M. Leighly[1], Hyunseop Choi (최현섭)[2], Michael Eracleous[3], Donald M. Terndrup[1,4], Sarah C. Gallagher[5,6,7], and Gordon T. Richards[8]
[1] Homer L. Dodge Department of Physics and Astronomy, The University of Oklahoma, 440 W. Brooks St., Norman, OK 73019, USA
[2] Département de Physique, Université de Montréal, Succ. Centre-Ville, Montréal, Québec, H3C 3J7, Canada
[3] Department of Astronomy & Astrophysics and Institute for Gravitation and the Cosmos, The Pennsylvania State University, 525 Davey Lab, University Park, PA, 16802, USA
[4] Department of Astronomy, The Ohio State University, 140 W. 18th Ave., Columbus, OH 43210, USA
[5] Department of Physics & Astronomy, The University of Western Ontario, London, ON, N6A 3K7, Canada
[6] Institute for Earth and Space Exploration, The University of Western Ontario, London, ON, N6A 3K7, Canada
[7] The Rotman Institute of Philosophy, The University of Western Ontario, London, ON, N6A 3K7, Canada
[8] Department of Physics, Drexel University, 32 S. 32nd St., Philadelphia, PA 19104, USA
Received 2023 September 11; revised 2024 February 28; accepted 2024 February 28; published 2024 April 26

Abstract

We present the optical–near-infrared spectral energy distributions (SED) and near-infrared variability properties of 30 low-redshift iron low-ionization Broad Absorption Line quasars (FeLoBALQs) and matched samples of LoBALQs and unabsorbed quasars. Significant correlations between the SED properties and accretion rate indicators found among the unabsorbed comparison sample objects suggest an intrinsic origin for SED differences. A range of reddening likely mutes these correlations among the FeLoBAL quasars. The rest-frame optical-band reddening is correlated with the location of the outflow, suggesting a link between the outflows and the presence of dust. We analyzed the WISE variability and provide a correction for photometry uncertainties in an appendix. We found an anticorrelation between the variability amplitude and inferred continuum emission region size, and we suggest that as the origin of the anticorrelation between variability amplitude and luminosity typically observed in quasars. We found that the LoBALQ Optical Emission-line and other parameters are more similar to those of the unabsorbed continuum sample objects than the FeLoBALQs. Thus, FeLoBAL quasars are a special population of objects. We interpret the results using an accretion-rate scenario for FeLoBAL quasars. The high-accretion-rate FeLoBAL quasars are radiating powerfully enough to drive a thick, high-velocity outflow. Quasars with intermediate accretion rates may have an outflow, but it is not sufficiently thick to include Fe II absorption. Low-accretion-rate FeLoBAL outflows originate in absorption in a failing torus, no longer optically thick enough to reprocess radiation into the near-IR.

Unified Astronomy Thesaurus concepts: Broad-absorption-line quasar (183); Quasars (1319); Spectral energy distribution (2129)

1. Introduction

Broad absorption lines observed in C IV are found in about 10%–26% of optically selected quasars (Tolea et al. 2002; Hewett & Foltz 2003; Reichard et al. 2003; Trump et al. 2006; Knigge et al. 2008; Gibson et al. 2009). These blueshifted lines reveal an unambiguous signature of outflow. Therefore, Broad Absorption Line Quasars (BALQs) may be important sources of quasar feedback in galaxy evolution. About 1.3% of quasars have broad Mg II absorption (Trump et al. 2006); these are called low-ionization broad absorption line quasars (LoBALQs). About 0.3% of quasars also have absorption from Fe II, and these are called iron low-ionization broad absorption line quasars (FeLoBALQs; Trump et al. 2006). FeLoBAL quasars are rare, and only a few were known before the Sloan Digital Sky Survey. For example, Hall et al. (2002) published spectra and discussed the wide range of features observed in 23 unusual objects discovered in the SDSS; many of those objects are FeLoBAL quasars.

How do BAL quasars, and FeLoBAL quasars specifically, fit in among quasars in general? Are FeLoBAL quasars fundamentally the same as all other BAL quasars, with their magnificent spectra being observed because of a select range of viewing angles? Or do FeLoBAL quasars mark a special stage in quasar evolution? Or are both factors important?

The spectral energy distribution provides a potentially powerful probe of quasar physics. Three components are generally observed: the accretion disk emission, typified by a blue optical-UV continuum spectrum; the torus, reprocessed continuum radiating in the infrared and identified by a break at 1 μm; and the X-ray emission, thought to originate in inverse Compton scattering of the accretion disk emission by energetic electrons. A range of relative strengths of these components are observed among active galactic nuclei (AGN) and quasars. For example, the prominence of the torus component relative to the optical power law has been observed to differ from object to object. While detailed models of the torus may be fit to extensive photometry data extending to the far-infrared (e.g., Lyu et al. 2017), fainter and less well-studied objects are limited to detection of the presence of hot dust that results in the upturn of the spectrum toward wavelengths just longward of 1 μm. Those that do not show this upturn are termed Hot-Dust Deficient (HDD), and Lyu et al. (2017) found

that HDD quasars have relatively lower accretion rates than other PG quasars. There may also be a connection between the presence of a hot dust component and BAL outflows; a strong hot-dust component has been found to be correlated with BAL strength (Zhang et al. 2014), C IV emission blueshift (Temple et al. 2021), and [O III] blueshift (Calistro Rivera et al. 2021).

Reddening from dust along the line of sight can also affect what we see, and it may also affect quasar selection. Quasars are most easily differentiated from stars by their blue optical band colors (e.g., Green et al. 1986); red quasars may be confused with low-mass stars. Modern data provide efficient selection of red quasars via their radio emission (e.g., Glikman et al. 2004) or WISE colors (e.g., Stern et al. 2012). They may also be detected spectroscopically (e.g., Klindt et al. 2019). Reddened quasars show a large range of interesting differences from the more typical blue quasars. For example, a larger fraction of LoBAL and FeLoBAL quasars are found among reddened quasars (Urrutia et al. 2009; Fynbo et al. 2013; Krogager et al. 2015, 2016). Reddened quasars have also been found to show excess near-infrared emission (Calistro Rivera et al. 2021) and blueshifted [O III] line emission (DiPompeo et al. 2018).

Reddening in quasars and BAL outflows has also been associated with quasar evolution (e.g., Urrutia et al. 2009). A popular scenario holds that quasar activity is initiated by mergers, with the early stages shrouded by dust (Sanders et al. 1988b; Hopkins et al. 2005). An object with a high accretion rate may be initially observed as a red quasar (e.g., Glikman et al. 2012). Such an object produces copious radiation that can destroy or eject the dust and reveal the brilliant quasar. Eventually, the fuel source decreases, turning off the quasar and the star formation, and producing a dormant early-type galaxy (e.g., Klindt et al. 2019). Some surveys of dust-reddened quasars have found a high fraction of LoBAL quasars, prompting the hypothesis that the LoBAL phenomenon is associated with young quasars (e.g., Urrutia et al. 2009). The discovery of an enhanced merger fraction in reddened quasars (e.g., Glikman et al. 2015) and LoBAL quasars (Lazarova et al. 2023) supports this idea.

Variability offers another way to probe the properties of quasars. It has long been known that the variability timescale is correlated with luminosity, or equivalently, that the variability amplitude is anticorrelated with luminosity. First shown in X-ray data (e.g., Barr & Mushotzky 1986; Green et al. 1993; Lawrence & Papadakis 1993; Nandra et al. 1997), this trend is now well established in the optical bandpass (e.g., Vanden Berk et al. 2004; Wilhite et al. 2008; Kelly et al. 2009; MacLeod & Ivezić 2010; Zuo et al. 2012; Gallastegui-Aizpun & Sarajedini 2014; Simm et al. 2016; Caplar et al. 2017; Sun et al. 2018; Laurenti et al. 2020; Suberlak & Ivezić 2021; De Cicco et al. 2022; Yu et al. 2022). Various authors assert a further dependence on Eddington ratio (e.g., Zuo et al. 2012; Simm et al. 2016; Yu et al. 2022) and/or black hole mass (e.g., Wilhite et al. 2008; Kelly et al. 2009; MacLeod & Ivezić 2010; Zuo et al. 2012; Suberlak & Ivezić 2021).

So far, our detailed studies have focused solely on FeLoBAL quasars, a fact that provokes the question: are the profound differences between FeLoBAL quasars and the unabsorbed matched comparison sample unique to FeLoBALQS, or are they shared by other BAL quasars? Confirmation that they are unique would support an evolutionary origin of the FeLoBAL quasar phenomenon.

Our paper is organized as follows. Because this paper is the fourth is a series, Section 2 gives a review of the principal results from the first three papers (Choi et al. 2022a, 2022b; Leighly et al. 2022). Section 3 describes the data used in this paper. Section 4 presents the extraction of characteristic properties used to describe the spectral energy distributions and the WISE variability. Section 5 describes the distributions of the extracted spectral energy distribution (SED) parameters and WISE variability parameters. Section 6 presents the results of correlations of the Optical Emission-line (Leighly et al. 2022) and *SimBAL* (Choi et al. 2022b) parameters with the SED and WISE variability parameters. Section 7 reports the results of the comparison of the optical emission-line properties of a sample of low-redshift LoBAL quasars with those of the FeLoBAL quasars and unabsorbed comparison sample presented in Leighly et al. (2022). Section 8 discusses the results of the analysis and presents a speculative scenario to explain the two groups of FeLoBAL quasars found in the first three papers of this series. Last, Section 9 gives a brief summary of results and conclusions.

Finally, we note special terminology used throughout the paper. We plot our spectra as a function of wavelength exclusively. We use the terms "steeper" or "bluer" when referring to spectrum or spectral energy distribution that is relatively brighter at short wavelengths, and "flatter" or "redder" for one that is relatively brighter at long wavelengths.

2. Brief Review of Papers I, II, and III

Choi et al. (2022b) [Paper I] reported the results of analysis of a sample of 50 low-redshift ($0.66 < z < 1.63$) FeLoBAL quasars using *SimBAL*. The forward-modeling spectral synthesis code *SimBAL* was introduced in Leighly et al. (2018); additional discussion and features are discussed in Leighly et al. (2019) and Choi et al. (2020).

The near-UV spectra of FeLoBAL quasars contain several to thousands of iron absorption lines, each characterized by its own critical density, excitation energy, and oscillator strength (e.g., Hall et al. 2002). Many investigators have used these lines and photoionization physics to analyze the properties of their outflows (Arav et al. 2001; de Kool et al. 2001, 2002a, 2002b; Everett et al. 2002; Arav et al. 2008; Korista et al. 2008; Moe et al. 2009; Bautista et al. 2010; Dunn et al. 2010; Aoki et al. 2011; Shi et al. 2016; Hamann et al. 2019). High densities (n) are recognized by the presence of lines from transitions with high critical density, while their absence signals a low-density outflow; in fact, an estimate of the density can be obtained by visual examination of the spectrum (Lucy et al. 2014). High ionization parameters U are recognized by the presence of transitions from relatively rare ions (e.g., from high energy levels that are difficult to populate in a photoionized gas), or from those with low oscillator strengths (e.g., Lucy et al. 2014). Such outflows require a large column density to build up a detectable absorption line that is obtained from a large ionization parameter, i.e., a large Strömgren sphere (e.g., Leighly et al. 2009). The robust measurements of U and n possible in FeLoBAL quasar spectra yield equally robust estimates of the location of the outflow, given by the standard formula ($R = \sqrt{Q/4\pi Unc}$). The difference between *SimBAL* and previous analyses is that *SimBAL* uses forward modeling, a venerable technique ubiquitously used in X-ray spectral modeling for decades. The advantage of forward modeling over inference in this context is that it can handle line blending

and makes use of constraints obtained by lines that are not present in the spectrum. As shown in Appendix C of Choi et al. (2022b), *SimBAL* produces values of the location of outflow that are commensurate with those obtained through inference methods.

Because of the rich information available in the rest near-UV spectra, the *SimBAL* analysis resulted in fully characterized outflows. The physical conditions of the outflow, including the ionization parameter, density, column density, and covering fraction, were measured for 60 outflow components (with some objects having more than one component). A principal result was that the FeLoBAL outflows are present at a large range of distances from the central engine ($0 \lesssim \log R \lesssim 4.4$ [pc]), with no evidence that disk winds (with $R \ll 0.01$ pc) are manifest as UV outflows. For most of the objects, the outflow velocity was inversely related to the distance from the central engine, as might be expected from radiative line driving. However, 11 objects had FeLoBAL gas lying less than 10 pc from the central engine with low ($v_{\rm off} > -2000\,{\rm km\,s^{-1}}$) outflow velocities. These objects were identified as "loitering outflow" objects that represent a newly discovered class of FeLoBALQs (Choi et al 2022b). This paper discussed the potential origins and acceleration mechanisms of FeLoBAL outflows as a function of distance from the active nucleus.

Among the 50 objects analyzed by Choi et al. (2022b), 30 had redshifts low enough ($z < 1$) that the Hβ and [O III] lines were visible in the spectra. Leighly et al. (2022) [Paper II] analyzed the rest-frame optical emission-line properties of these spectra, focusing on the rich diagnostic information obtainable from the Hβ/[O III]/Fe II region. A comparison sample of 132 unabsorbed quasars matched in redshift, signal-to-noise ratio (S/N), and luminosity was analyzed in parallel. The description of the construction of the comparison sample may be found in Section 2.1 of Leighly et al. (2022). They found the anticorrelation between [O III] equivalent width and Fe II/Hβ that is ubiquitous in quasars. They developed a summary statistic called $E1$ (Figure 3 and Section 3.1 in Leighly et al. 2022) that characterizes this anticorrelation. They found that, while the unabsorbed objects showed a single-peak distribution of $E1$, the FeLoBALQs showed a broader and double-peaked distribution. $E1$ is strongly correlated with accretion rate (Leighly et al. 2022, Figure 12), implying that low-redshift FeLoBALQs are characterized by either a low accretion rate ($E1 < 0$) or a high accretion rate ($E1 > 0$). In addition, Leighly et al. (2022) reported that the Hβ FWHM width is systematically larger in FeLoBAL quasars than in unabsorbed objects (Leighly et al. 2022, Section 3.4.1, Figure 13), implying a larger-inclination viewing angle *or* a consequence of diminished emission in the core of the line profile.

Finally, Choi et al. (2022a) [Paper III] compared the results of the *SimBAL* analysis presented in Paper I with the results of the optical emission-line analysis in Paper II. They found that the outflow properties were also correlated with the accretion rates. The high-accretion-rate objects showed faster outflows closer to the central engine, while the low-accretion-rate objects (the loitering outflow objects among them) showed near-zero outflow velocities close to the central engine, and higher velocities at large distances (Choi et al. 2022a, Figure 4). High-accretion-rate objects showed outflows with significantly lower volume-filling factors than the low-accretion-rate objects. These results are especially profound among the objects with smaller-scale ($\log R < 2$ [pc]) outflows, and provide further support that, at least for the smaller-scale outflows, there are two populations of FeLoBAL quasars.

3. Data

Most of the data and analysis results used in this paper were taken from Choi et al. (2022b), Leighly et al. (2022), and Choi et al. (2022a). Additionally, in this paper, we include broadband photometry from the 30 low-redshift FeLoBALQs and the comparison sample identified in Paper II (Section 3.1), the WISE and NEOWISE photometry (Section 3.2), measurements of the Optical Emission-lines from a sample of LoBAL quasars (Section 3.3), and an IRTF observation of SDSS J144800.15+404311.7 (Section 3.4).

3.1. Spectral Energy Distributions

We compiled the photometry information for the FeLoBALQs and comparison sample from SDSS (Blanton et al. 2017), 2MASS (Skrutskie et al. 2006), UKIDSS (Lawrence et al. 2007), and WISE (Wright et al. 2010). In a very few cases, we also included GALEX (Martin et al. 2005). These data were corrected for redshift using the values presented in Leighly et al. (2022) and Milky Way reddening (Cardelli et al. 1988). The results are shown in Figure 1. If both UKIDSS and 2MASS data were available, the higher-sensitivity UKIDSS data are shown.

At low redshift and low luminosity, the host galaxy may contribute significantly to the spectral energy distribution. To determine whether galaxy subtraction is necessary, we made a zeroth-order estimate of the contribution of the host galaxy to the photometry using Equation (1) of Richards et al. (2006). This relationship, adapted from Vanden Berk et al. (2006), relates the luminosity density of the quasar at 6156 Å to the luminosity density of the host galaxy at the same wavelength after adjusting for the Eddington ratio. We estimated the luminosity density of the quasar from the photometry fits described below. We used the Eddington ratios from Leighly et al. (2022). A 5 Gyr old elliptical template from the SWIRE template library (Polletta et al. 2007) was scaled to the galaxy flux-density estimates, and these are shown in Figure 1. With the exception of one or two cases where the luminosity and accretion rate are low, the quasar is very much brighter than the host galaxy. Because one of the criteria defining the unabsorbed comparison sample was the luminosity, which was based on the 3 μm flux density (Leighly et al. 2022), we expect very similar properties for the comparison sample. We therefore do not correct the photometry for the host-galaxy emission.

The SEDs of the FeLoBALQs show a wide range of shapes. There are some objects that appear indistinguishable from a slightly reddened average quasar (e.g., SDSS J104459.60+365605.1 and SDSS J103036.92+312028.8) or a somewhat more reddened average quasar (e.g., SDSS J080248.18+551328.8). Others have more peculiar SEDs. Several Seyfert 1.8 objects show an abruptly flatter optical spectrum shortward of ~6000 Å than the extrapolated optical-to-infrared slope would predict (e.g., SDSS J120049.54+632211.8 and SDSS J124014.04+444353.4). Finally, some objects lack the upturn toward longer wavelengths expected from the torus (e.g., SDSS J080957.39+181804.4 and SDSS J121442.30+280329.1).

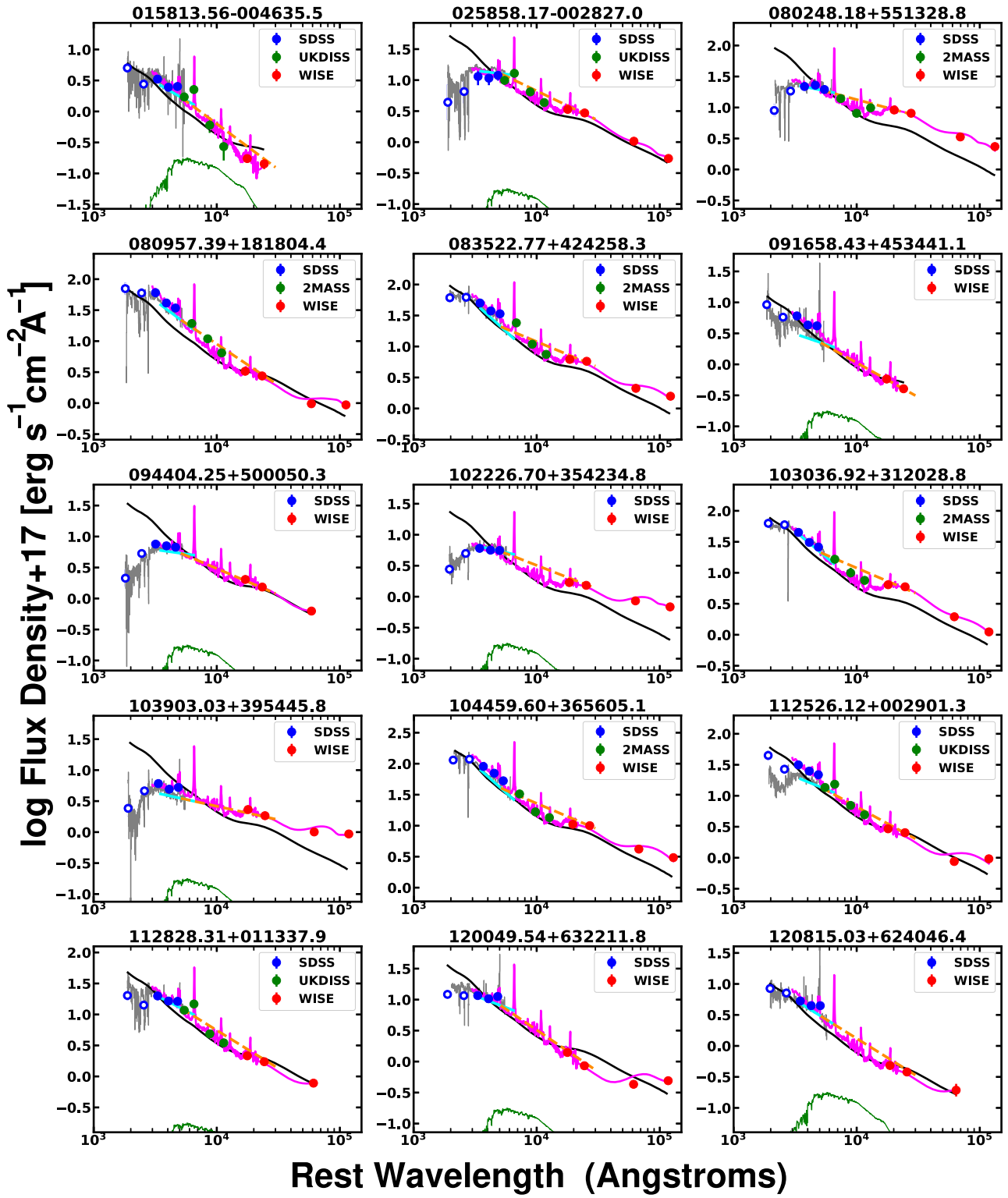

Figure 1. Photometry spectral energy distributions of the FeLoBALQ sample. The magenta line shows the empirical model (Section 4.2), while the black line shows the Krawczyk et al. (2013) continuum normalized to the model continuum at 9730 Å, and the gray line shows the heavily rebinned spectrum. The green line shows the estimated contribution of the host galaxy, which is weak or absent in most cases. Open markers denote points not used in the SED fitting. The orange dashed (cyan solid) lines show α_{oi} (power-law index) defined in Section 3.1. The SED shapes range from a simple SMC-reddened Seyfert (e.g., SDSS J080248.18+551328.8) to objects that appear to lack a near-infrared bump (e.g., SDSS J080957.39+181804.4) to objects with very red optical spectra (e.g., SDSS 124014.04+444353.4).

3.2. WISE Photometry Variability

We used WISE photometry to investigate the near-IR variability of the FeLoBALQs and the comparison sample between 2010 and 2020. We used *unTimely*, the time-domain catalog of detections from the Wide-field Infrared Survey Explorer (WISE) and NEOWISE missions. The catalog was constructed from the time-resolved unWISE coadded images, i.e., the stacked images from each biannual pass (Meisner et al. 2023).

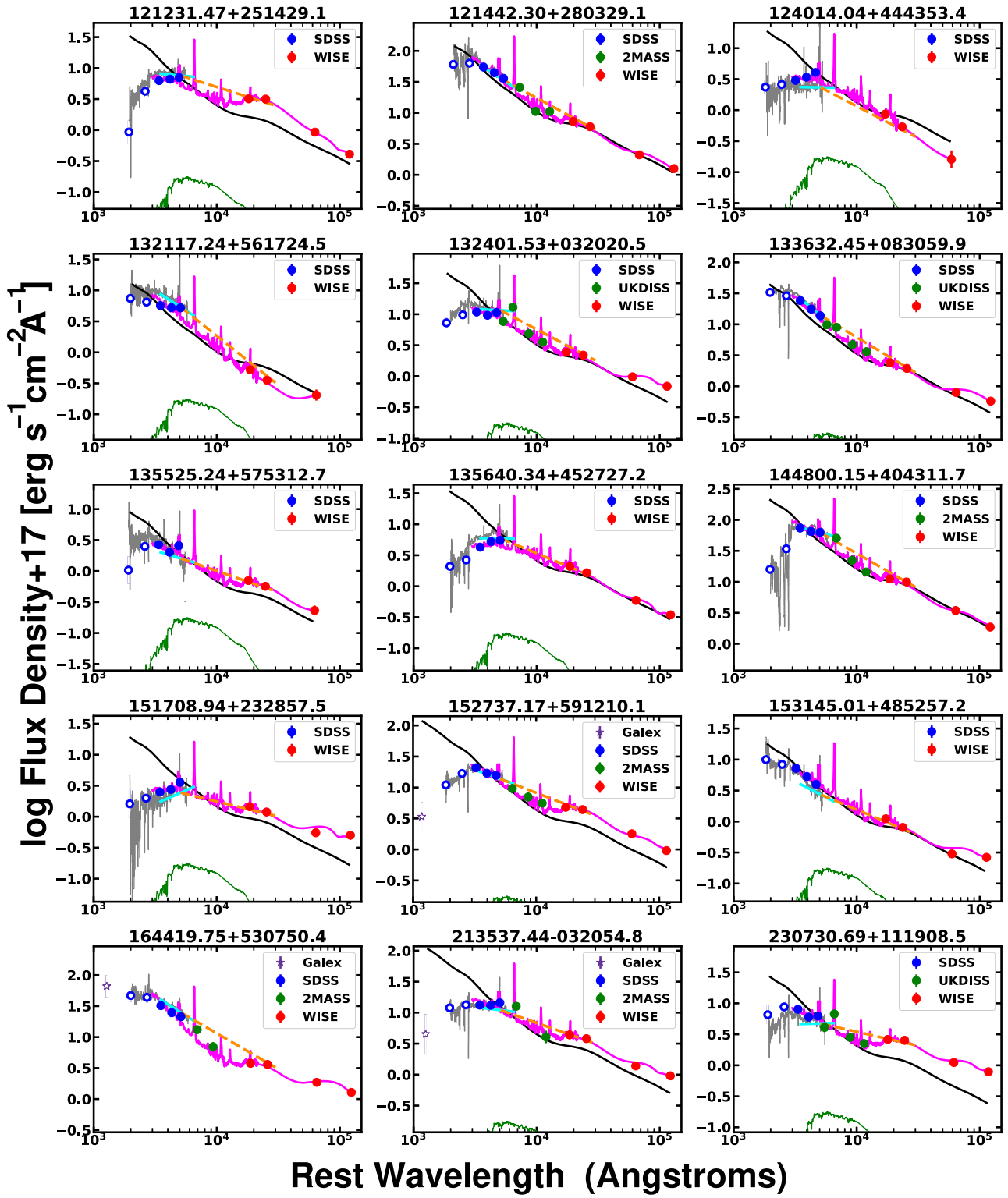

Figure 1. (Continued.)

The catalog yields mid-infrared lightcurves from the W1 and W2 WISE filters (3.4 and 4.6 μm), respectively. The sampling rate and duration are very uniform: every six months between 2010 and 2020, with the exception of a three-year gap between the WISE and NEOWISE missions; each lightcurve includes 16 or 17 points. For the $0.8 \lessapprox z < 1.0$ objects investigated in this paper, the 10 yr time span is equivalent to about 5 yr at $\sim$1.8 and $\sim$2.5 μm in the rest frame. The lightcurves sample principally the hot-dust component of the torus and secondarily the accretion disk emission extending into the near-infrared.

We downloaded the data using the `unTimelyCatalogExplorer` (Kiwy 2022). We investigated the variability properties by selecting star candidates ($-0.2 < \mathrm{W1} - \mathrm{W2} < 0.2$) in a 500″ region around the targets with magnitudes similar to

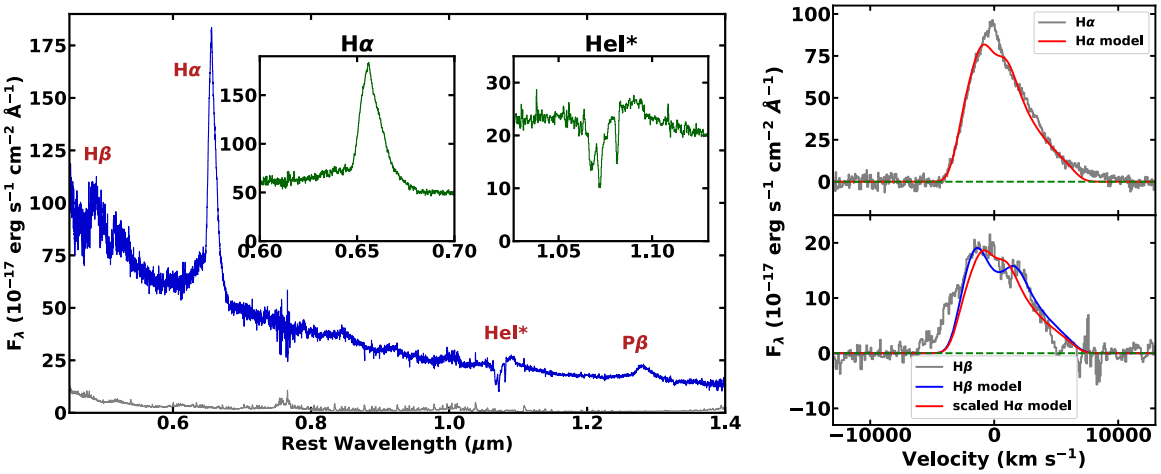

Figure 2. Left: The IRTF *SpeX* spectrum of SDSS J144800.15+404311.7. Principal emission lines are labeled. The inset panels highlight the unusually shaped Hα line and the He I$^*\lambda$10830 absorption line. Right: The Hα emission line from an IRTF SpeX observation of SDSS J1448+4043 is fit well by a disk-line profile plus a very broad and blueshifted pedestal (not shown). The Hβ line can also be modeled with the disk-line profile.

those of the targets. Most classes of stars are not substantially variable. However, analysis of the star properties found that the lightcurves were significantly variable. This result implies that the errors in the catalog are underestimated. We devised a correction of the errors. This analysis and the revised errors are given in the Appendix.

3.3. A Sample of LoBAL Quasars

In Leighly et al. (2022), we analyzed the optical properties of a sample of FeLoBAL quasars with redshifts less than 1.0. At these redshifts, the rest-frame emission lines between ∼3500 and ∼5500 Å may be modeled if the bandpass extends to sufficiently long wavelengths and if the sky emission, which dominates observed-frame emission longward of ∼8000 Å, is cleanly subtracted. While this redshift range is far too low to identify high-ionization BAL quasars, it is low enough that LoBAL quasars can be identified, and the same analyses performed on them.

We used the SDSS DR12 BAL quasar catalog (Pâris et al. 2017) to build a sample of LoBAL quasars. To match the comparison sample used in Leighly et al. (2022), we chose the redshift range $0.75 < z < 1.0$ (Leighly et al. 2022, Figure 2). We found 176 objects in that redshift range. The 29 FeLoBAL quasars were excluded. Another 57 were rejected because they did not show evidence for Mg II absorption. In many cases, the objects were extreme iron emitters, and the strong upturn near 2600 Å was apparently identified as recovery from a longer-wavelength absorption line (e.g., Leighly & Moore 2006, Figure 6). An additional 26 were excluded because the long-wavelength region was too noisy to analyze. In the end, the spectra of 66 LoBALQs were analyzed.

3.4. IRTF Observation of SDSS J1448+4043

SDSS J144800.15+404311.7 was observed using IRTF *SpeX* (Rayner et al. 2003) as part of program 2015A041 on 2015 May 1 for a total exposure time of 40 minutes using a 0.″8 slit and the short-wavelength cross-dispersing grating. The near-infrared observation was done to observe the predicted metastable He I$^*\lambda$10830 absorption line. A standard ABBA integration scheme was used. The A0 star HD 128039 was used for flux and telluric corrections. The spectra were reduced and the telluric correction applied in the standard manner using `Spextool` and accompanying software (Vacca et al. 2003; Cushing et al. 2004). The spectrum was corrected for reddening using $E(B-V) = 0.011$ (Schlafly & Finkbeiner 2011) and redshift using $z = 0.805$ (Pâris et al. 2018).

The full spectrum is shown in Figure 2. The left inset panel shows the Hα line, which has a unusual shape in this object. It is not symmetric; it has an extended blue wing and a steeply rising blue side, with a gradual decline toward longer wavelengths. While red wings have been observed in Balmer lines from AGNs previously (e.g., La Mura et al. 2009), the steep blue side is rare. This profile is an example of line emission from an accretion disk viewed at a low angle from the normal (e.g., Figure 2 of Chen & Halpern 1989). The right inset panel shows the He I$^*\lambda$10830 absorption line. The shape matches that of the He I$^*\lambda$3889 absorption line, and it very roughly corresponds to the *SimBAL* inferred opacity for the Mg II absorption.

4. Preliminary Analysis

We introduced the data used in this paper in Section 3. In this section, we extract parameter measurements that characterize the data and can be used to compare among samples, including parameters characterizing the accretion rate and outflow properties.

4.1. Spectral Energy Distributions: Parameters

We compiled five empirical measurements to describe the shape of the continuum; these are described in Table 1 and illustrated in Figure 3. The effective power-law index between 4500 and 5500 Å was constructed from the continuum component of the spectral fitting model presented in Leighly et al. (2022). We also defined α_{oi}, the point-to-point flux density slope between 5100 Å, also extracted from the spectral fitting model, and the 3 μm flux density interpolated from the WISE photometry. Both of these parameters are potentially sensitive to both reddening and intrinsic differences in spectral shape. The third parameter is WISE W1−W2 in magnitude units. Most of our objects have redshifts between 0.8 and 1.0, which means that W1 and W2 measure the flux densities near 1.7–1.86 and 2.3–2.56 μm, respectively. The values fall on the upturn from the 1 μm dust sublimation break toward the torus infrared bump; see, for example, the Krawczyk et al. (2013)

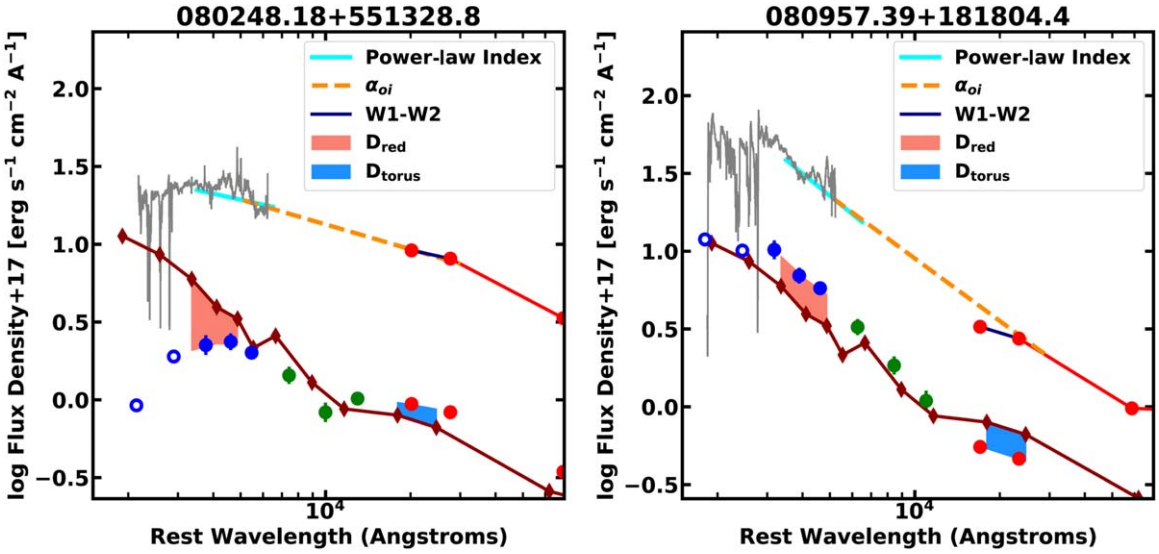

Figure 3. Illustrative example of defined photometry parameters. The solid circular points show the flux densities derived from the photometry, the gray line shows the heavily rebinned spectrum, and the dark red line and red diamonds show the composite photometry spectrum from the unabsorbed objects. The upper plot shows parameters defined in the rest frame for each object individually (the power-law index, α_{oi}, and W1−W2), while the lower one shows the parameters defined from the normalized spectra ($D_{\rm red}$ and $D_{\rm torus}$). The colored patches show the regions of the spectra where the $D_{\rm red}$ and $D_{\rm torus}$ parameters are defined; see text and Table 1 for details. The left panel shows an example of an overall flat spectrum with negative $D_{\rm red}$ due to significant reddening and positive $D_{\rm torus}$ due to a prominent torus. The right panel shows an overall steep (blue) spectrum with positive $D_{\rm red}$ and negative $D_{\rm torus}$.

Table 1
Continuum Parameter Definitions

Parameter Name	Computational Defintion	Utility and Interpretation
Power-law Index	$\frac{\log_{10}(F_\lambda(5500)) - \log_{10}(F_\lambda(4500))}{\log_{10}(5500) - \log_{10}(4500)}$	Local optical continuum index[a]
α_{oi}	$\frac{\log_{10}(F_\lambda(30000)) - \log_{10}(F_\lambda(5100))}{\log_{10}(30000) - \log_{10}(5100)}$	Overall optical-NIR continuum shape[b]
W1−W2	W1 − W2	Color that measures the strength of 1 μm upturn
$D_{\rm red}$	$\frac{1}{3}\sum_{r,i,z}(\log_{10} F_{\rm obs} - \log_{10} F_{\rm composite})$	Isolates the relative optical band reddening[c]
$D_{\rm torus}$	$\frac{1}{2}\sum_{W1,W2}(\log_{10} F_{\rm obs} - \log_{10} F_{\rm composite})$	Isolates the relative torus strength[c]

Notes.
[a] Computed from the continuum portion of the optical emission-line models presented in Leighly et al. (2022).
[b] Computed from interpolations of the log flux density from the photometry.
[c] The composite SED constructed from the unabsorbed sample, as described in Section 4.2.

composite spectrum. Therefore, the W1−W2 color is a measurement of the prominence of the hot dust portion torus in the SED; a larger value of W1−W2 implies that the spectrum is flatter (redder) and the torus is more prominent. The final two parameters are defined in Section 4.2.

4.2. Spectral Energy Distributions: Composites

The empirical parameters have the advantage that they can be robustly measured from the SEDs. However, their interpretations may be ambiguous. For example, the α_{oi} parameter may be larger (flatter or redder) either because of reddening or because of strong hot dust and torus emission. To address this limitation, we also perform photometry SED fitting to the rest-frame optical through near-IR bands, and use the results, as described below and as illustrated in Figure 3, to separate the contributions of the rest-frame infrared and optical bands to α_{oi}.

We used the simplified and parameterized model described by Temple et al. (2021) on the F_λ SED spectra, modified appropriately for our BAL quasar data. Their model consisted of a broken power law with fixed break wavelength at 2820 Å and indices of −1.52 and −1.84 for the short and long wavelengths, respectively. To that, they added line emission extracted from the UV-optical template from Francis et al. (1991) and the NIR template from Glikman et al. (2006) and convolved with the relevant filter curves. They added a blackbody component with fixed temperature $T = 1280$ K. The result was convolved with an SMC reddening curve. The torus emits over a broad wavelength range, and it cannot be modeled using a single blackbody when the WISE W3 and W4 points are present. We included a second blackbody component with fixed temperature $T = 350$ K, when necessary, to model the WISE W3 and W4 points. The free parameters were therefore the normalizations of the fixed-shape optical continuum and the two blackbodies, as well as the SMC $E(B-V)$, which was allowed to take negative as well as positive values to model spectra both intrinsically steeper (bluer) and flatter (redder) than the fixed broken power-law values. Following Temple et al. (2021), the photometry error minimum is assigned to be 0.05 mag.

Although we used the same model as Temple et al. (2021), our analysis differed somewhat because our data are more limited. All of the objects in the Temple et al. (2021) sample

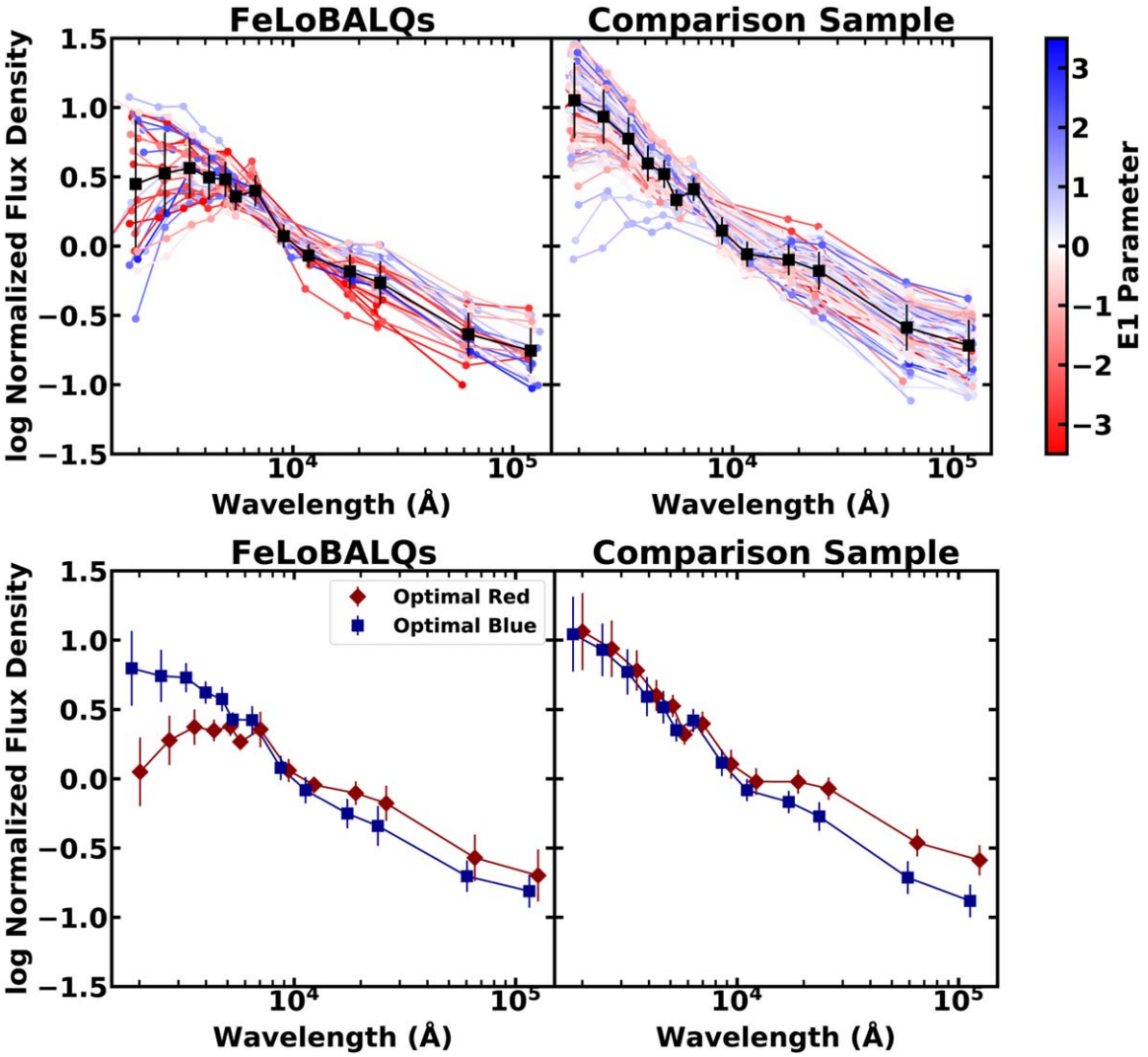

Figure 4. Top: The normalized photometry for the FeLoBAL quasars (left) and the comparison spectrum (right) colored according to the $E1$ parameter (defined in Section 2 in Leighly et al. 2022). Overlaid are the mean normalized spectra binned by filter, where the error bars show the standard deviation of the points. Bottom: The optimal red and optimal blue spectra constructed from the FeLoBALQs and comparison sample spectra as described in the text. The points are slightly shifted in wavelength for plot clarity. The peak near 6500 Å is Hα. Both sets of objects show significant variance in their near-IR components. The FeLoBALQs clearly show deficits at the shorter wavelengths, consistent with reddening.

were required to have UKIDSS photometry, a fact that meant that the models were well constrained near the crossover point between the broken power law modeling the accretion disk emission at shorter wavelengths and the blackbody modeling the torus emission at longer wavelengths. In contrast, only 7 of our 30 low-redshift FeLoBAL quasars had UKIDSS photometry, and 13 lacked any near-infrared photometry. Also, we ignored WISE photometry points with S/Ns less than 3. Finally, we only fit longward of 3000 Å, to avoid the BAL absorption. The result is that there are objects that have as few as five photometry points fit, a fact that might result in model dependence. We therefore adopted the following approach to parameterize our data: we used the model fit parameters to provide the normalization at 1 μm so that we could create composite spectra, and then compared the model fit results of the individual objects to the composite spectra.

For objects in our redshift range, the J, H, and K bands correspond approximately to rest frame 6500, 8750, and 11300 Å (computed for $z = 0.9$), i.e., spanning our 1 μm normalization point. Because many of our objects lack near-infrared photometry, we first investigated whether the model fits provided sufficiently robust normalizations at 1 μm. We tested this by fitting all of the comparison sample objects that have NIR photometry (62 objects), and then repeating the model fitting with the NIR points removed. We found that the mean of the ratio of the no-IR-photometry normalization factor to the nominal one was 1.008, with a standard deviation of 0.09, i.e., about 10%. Considering that we performed our subsequent analysis on the log of the flux densities, this small uncertainty was deemed acceptable. We speculate that the highly constrained nature of the model and the limited redshift range of the targets is the origin of the small uncertainty. Specifically, the fixed-temperature blackbody normalizations were well constrained by the WISE data, while the normalization and reddening of the fixed-shape continuum component were well constrained by the SDSS photometry.

Armed with the normalized photometry, we proceeded to make composite spectra. Because of the limited redshift range, we could average filter by filter without any K-correction. We used a straight average rather than a weighted average, to avoid bias toward brighter objects. Figure 4 shows all of the

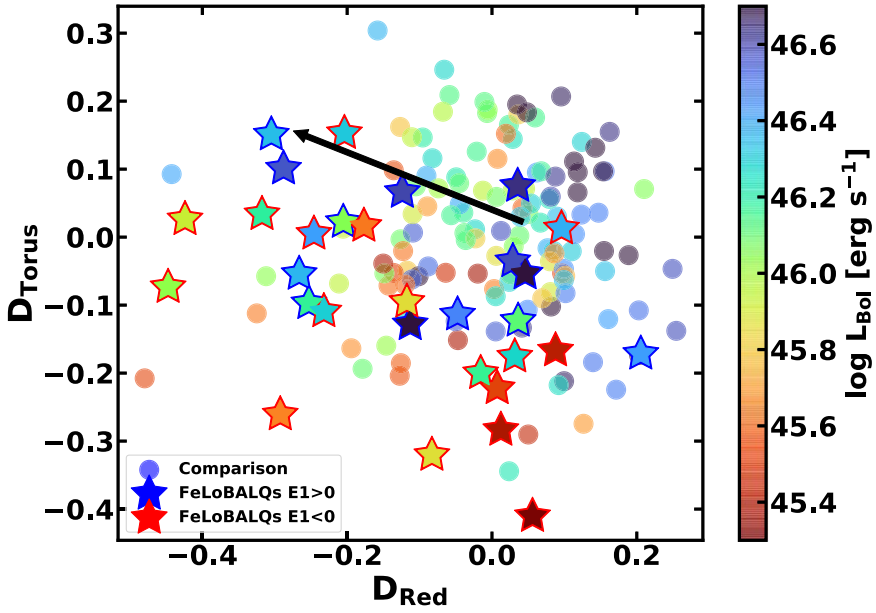

Figure 5. The $D_{\rm torus}$ parameter as a function of the $D_{\rm red}$ parameter. The black arrow shows the prediction for the Krawczyk et al. (2013) composite spectrum for $A_V = 0$ to $A_V = 1$. The normalization of the SEDs at 1 μm predicts that, if the SED shape differences are dominated by differences in reddening, then these two parameters should be tightly anticorrelated. No correlation or trend is present among these two parameters, indicating that other factors must contribute to the range in SED shapes.

normalized photometry and the mean spectra for both the comparison sample data and the FeLoBAL quasar spectra.

The photometry SEDs show a range of shapes, and it appears that these are not obviously correlated with the $E1$ parameter (defined in Section 2 in Leighly et al. 2022). In the optical band, the spectral shape range seen in Figure 4 could be due to differences in reddening or the variations in the intrinsic slope of the power law. In the near-infrared, the relative strength of the hot dust component may change the spectral shape (e.g., Temple et al. 2021). We defined two deviation parameters, one in the optical band called $D_{\rm red}$, and another in the near-infrared band called $D_{\rm torus}$. For $D_{\rm red}$, we used the SDSS r, i, and z measurements; the shorter bands were ignored because they may be contaminated by the BALs. For $D_{\rm torus}$, we used WISE W1 and W2 because those data exist for the entire sample; some objects are not detected in WISE W3 and W4. To create these deviation parameters, we first performed a linear interpolation on the log flux densities from each object onto the wavelengths from the composite spectrum of the comparison sample. The deviations were computed as the mean difference between the log of the normalized flux densities inferred from the photometry and the log of the corresponding flux densities of the composite spectrum (i.e., from the three values in the optical band and from the two values in the near-infrared). These parameters are illustrated in Figure 3, and their definitions are given in Table 1.

The sign of the deviation indicates whether the photometry lies above the composite model (positive) or below it (negative). By definition, the means of $D_{\rm red}$ and $D_{\rm torus}$ are very close to zero for the comparison sample. The standard deviations for the comparison sample are 0.13 and 0.12 for $D_{\rm red}$ and $D_{\rm torus}$, respectively. In contrast, the mean of $D_{\rm red}$ for the FeLoBALQs is -0.12, implying that FeLoBALQs are generally more reddened than unabsorbed objects. Reddening is known to be more prevalent among BAL quasars compared with unabsorbed objects (e.g., Krawczyk et al. 2015, and references therein), so this result is no surprise. The standard deviation is 0.17 for the FeLoBALs, implying there is also more scatter than among the comparison objects. Indeed, 11 objects (1/3 of the sample) have $D_{\rm red} > 0$. Likewise, the mean of $D_{\rm torus}$ for the FeLoBALQs is -0.08, which implies that the torus emission in the FeLoBALQs is weaker than among the unabsorbed quasars. The standard deviation of $D_{\rm torus}$ for the FeLoBALQs is 0.14, comparable to that of the unabsorbed quasars, and 11 objects (1/3 of the sample) show positive values of $D_{\rm torus}$.

Normalization at 1 μm might lead to an apparently stronger torus contribution in reddened objects compared with, for example, a normalization at longer wavelengths. That is, reddening attenuates the spectra at all wavelengths, but more toward shorter wavelengths. Tilting a spectrum down at all wavelengths, then normalizing at 1 μm, effectively tilts the near-IR spectrum up a small amount. Thus, $D_{\rm red}$ and $D_{\rm torus}$ should be anticorrelated if reddening dominates the spectral variability. However, there is no evidence for an anticorrelation (see Figure 5, Section 6.1, and Figure 9). Therefore, while reddening must influence the SED shapes to some degree, it does not dominate the spectral variance in the sample.

We were able to divide the redder and blue spectra into two groups from which we made composite spectra. This was done using an expectation/maximization algorithm.[9] First, seed red and blue composites were made based on the α_{oi} values. We then computed the mean squared distance of the photometry points from the seed spectra (expectation step). The results were divided into two groups of objects: those that were closer to the red spectrum and those that were closer to the blue spectrum, according to our metric (maximization step). New composite spectra were computed from those groupings, and the process iterated until it converged. The process was performed separately for the FeLoBALQs and the comparison sample quasars. The results are termed optimal red and optimal

[9] E.g., https://en.wikipedia.org/wiki/Expectation-maximization_algorithm.

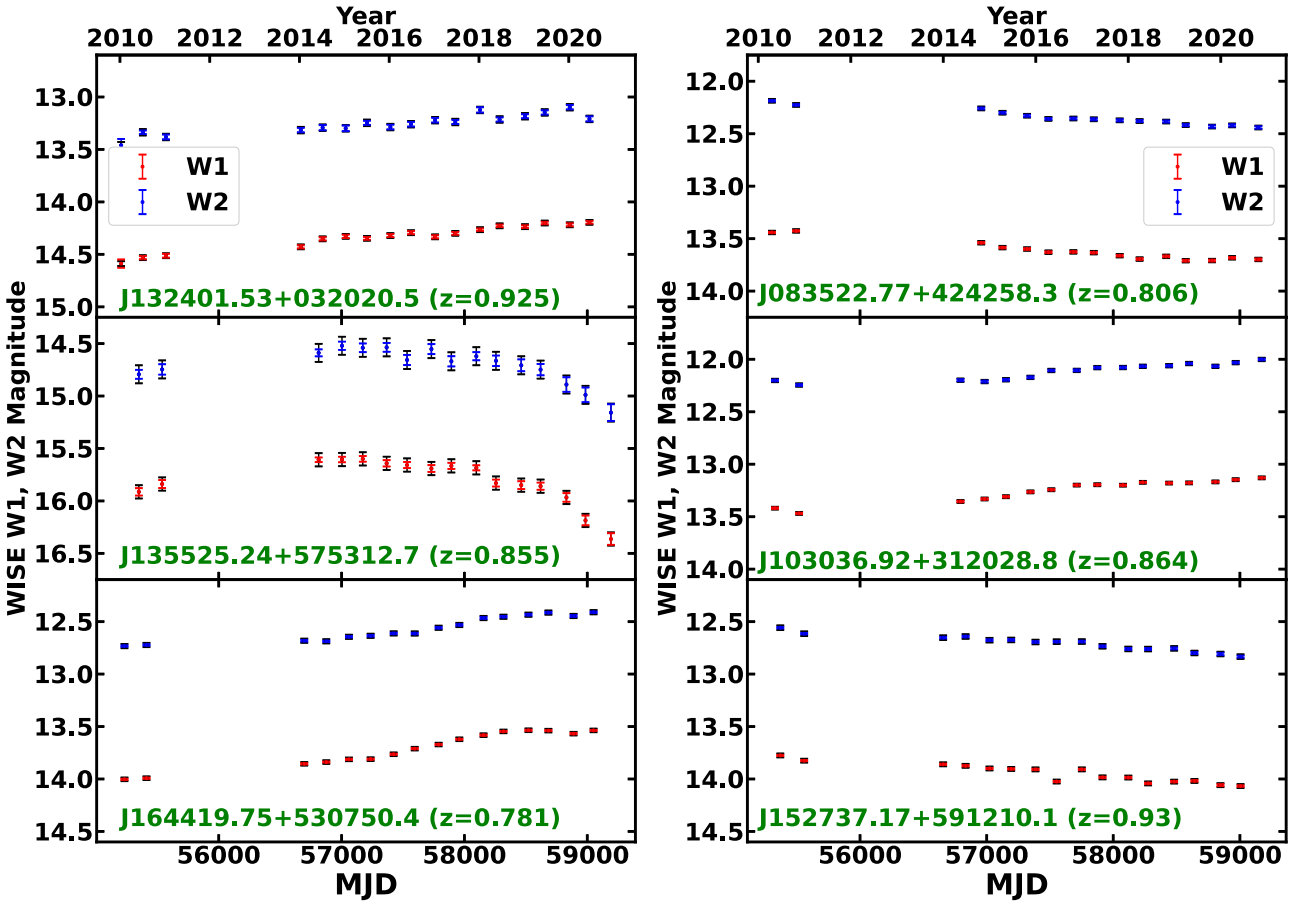

Figure 6. WISE W1 and W2 lightcurves of six of the more variable FeLoBALQs. Left: objects with $E1 < 0$. Right: objects with $E1 > 0$. The colored error bars show the photometry errors obtained from the unTimely catalog, and the black error bars show the systematic errors derived using the scheme presented in the Appendix. The lightcurves are given in the observed frame spanning about 10.5 yr. The redshifts of these objects are mostly between 0.8 and 1, yielding rest-frame lightcurves spanning about 5 yr.

blue composite spectra; they are shown in the lower panel of Figure 4. As before, points shortward of 3000 Å were ignored for all the spectra, to avoid the contamination of the broad absorption lines.

We found that the optimal red and blue spectra from the comparison sample differed only at long wavelengths, implying that the variance among the SEDs from unabsorbed objects is principally due to variance in the prominence of the hot dust emission. In contrast, the FeLoBALQs differed both at short wavelengths and at long wavelengths, suggesting that both reddening and prominence of hot dust emission are important.

4.3. WISE Variability Analysis

We constructed four parameters to describe the variability properties. The principal measures were the excess variance of the W1 and W2 lightcurves. The excess variance is the variance of the magnitude lightcurve corrected for the variance due to noise by subtracting the mean error squared. The equation for excess variance is given as

$$\mathrm{EV} = \mathrm{Variance(Magnitude)} - \mathrm{Error(Magnitude)}^2,$$

where Variance(Magnitude) is the measured variance in the magnitudes, and Error(Magnitude)^2 represents the variance due to corrected statistical uncertainty. The excess variance has a long history in the studies of AGN X-ray variability (e.g., Nandra et al. 1997; Leighly 1999), and it has more recently been used to characterize optical variability (e.g., López-Navas et al. 2023). The errors on the excess variance were taken to be the 1σ bounds of the systematic error described in Appendix. We found that most of the objects were variable. Of the FeLoBALQs, 83% (70%) showed excess variance $\mathrm{EV_{W1}}$ ($\mathrm{EV_{W2}}$) more than 3σ larger than zero, while 85% (64%) of the comparison sample showed $\mathrm{EV_{W1}}$ ($\mathrm{EV_{W2}}$) more than 3σ larger than zero. Lightcurves of the six FeLoBALQs with the highest-S/N excess variance measurements are shown in Figure 6. The variability is characterized by smooth increases or decreases by a few tenths of a magnitude.

The third parameter was the color excess variance, i.e., the difference between $\mathrm{EV_{W1}}$ and $\mathrm{EV_{W2}}$. The errors were propagated using the Monte Carlo scheme described in Leighly et al. (2022). Specifically, 10,000 normally distributed values scaled to the positive and negative uncertainties were created for each measurement. The difference between each pair of values was computed, and the error was taken to be the 16% and 84% cumulative bounds on the resulting distribution. A positive (negative) value of the color excess variance indicates that the amplitude of variability is larger (smaller) in W1 than in W2. The final parameter measured the correlated variability between the W1 and W2 lightcurves, and it was defined as the probability that a correlation would be detected in variations solely due to statistical fluctuations.

4.4. Rest-frame Optical Band Spectral Fitting of a Sample of LoBAL quasars

The sample of 62 LoBAL quasar spectra was analyzed following Leighly et al. (2022). Specifically, the optical emission-line region was analyzed using *Sherpa* (Freeman et al. 2001) using a model including a power-law continuum, Balmer emission lines, [O III] emission lines, and a template model for Fe II; see Section 2.2 of Leighly et al. (2022) for details. The spectra were also analyzed using the PCA eigenvectors developed in Leighly et al. (2022). Because eigenvector model fitting uses correlated features over a broad bandpass, this type of analysis can be less dependent on individual features and therefore can be more robust when the S/N is low.

4.5. Accretion Disk Models of SDSS J1448+4043

We fitted the profile of the Hα line of SDSS J1448+4043 with a model that attributes the line emission to an annulus in the accretion disk. The model, developed by Chen et al. (1989) and Chen & Halpern (1989), includes relativistic effects, such as light bending, Doppler boosting, and transverse and gravitational redshift. The disk is circular and inclined so that its axis makes an angle i with the line of sight. The line-emitting annulus is bound between inner and outer radii ξ_1 and ξ_2, expressed in units of the gravitational radius, $r_g = GM_{BH}/c^2$, where M_{BH} is the mass of the black hole. The lines originate in a photoionized surface layer in the disk with an emissivity that varies as a power law with radius $\epsilon(\xi) \propto \xi^{-q}$. The combination of all local broadening mechanisms, such as turbulence in the emission layer and scattering, is captured by a Gaussian local line profile of velocity dispersion σ (referred to as the broadening parameter). Thus, the model has five free parameters: the inclination angle of the disk, i; the inner and outer radii of the line-emitting region, ξ_1 and ξ_2; the emissivity power-law index, q; and the broadening parameter, σ. The inclusion of relativistic effects, especially the transverse and gravitational redshifts, makes the line profile asymmetric and breaks the classical degeneracy between the radius and the inclination angle. As a result, fitting the model to an observed line profile allows for the determination of ξ_1 and ξ_2 separately from i.

The best-fitting model is shown in the right panel of Figure 2 as a magenta line superposed on the observed profile of the Hα line. The model was scaled to match the wings of the line while missing the narrow Hα+[N II] complex, and compared by eye to the observed line Hα profile. The parameters were then adjusted iteratively until a good fit was achieved. Uncertainties on the model parameters were determined by progressively perturbing their values about the best fit and adjusting other parameters to compensate. Thus, we obtained an inclination angle of $i = 15° \pm 2°$, inner and outer radii of the line-emitting portion of the disk of $(\xi_1,\ \xi_2) = (240,\ 9500) \pm 10\%$, an emissivity power-law index of $q = 2.4 \pm 0.1$, and a broadening parameter of $\sigma = 600 \pm 200\ \mathrm{km\ s^{-1}}$. The disk is viewed close to face-on in the context of this model. The pronounced red wing is the result of substantial transverse and gravitational redshifts of photons emitted near the inner radius.

The lower panel of the right side of Figure 2 shows the profile of the Hβ line after subtraction of the Fe II complex and plotted on the same velocity scale as the Hα line. The magenta line shows the model that fits the Hα line on the same velocity scale as Hβ. Although the Hβ profile is noisier, the Hα model does not describe it very well; the Hβ profile is somewhat broader than that of Hα, which is a well-known trend (see Stirpe 1991, and references therein). The agreement between the model and the Hβ profile improves if we assume that the line emitting region is more centrally concentrated by reducing the outer radius to $\xi_2 = 3200$ and changing the emissivity power-law index to $q = 2.3$. The improved model is shown as a blue line in the lower panel of Figure 2. Such a modification to the model is consistent with theoretical expectations for the line emissivity of photoionized accretion disks (Dumont & Collin-Souffrin 1990).

5. Distributions of the SED and WISE Variability Parameters

In this section, we compare the SED and WISE variability properties between the FeLoBALQ and unabsorbed comparison samples. Following Leighly et al. (2022), we present the comparison for the full sample, and also for the $E1 > 0$ and $E1 < 0$ subsamples. As in Leighly et al. (2022) and Choi et al. (2022b), we used the two-sample Kolmogorov–Smirnov (KS) test and the two-sample Anderson–Darling (AD) test. The KS test reliably tests the difference between two distributions when the difference is large at the median values, while the AD test is more reliable if the differences lie toward the maximum or minimum values (i.e., the median can be the same, and the distributions may differ at larger and smaller values).[10] The parameter value and false-alarm probabilities for these tests are included in Table 2.

5.1. SED Parameters

The cumulative probability distributions of the SED parameters are shown in Figure 7. We found that the power-law index between 4500 and 5500 Å measured from the continuum model fits under the Hβ/[O III]/Fe II model is significantly flatter (redder) for all of the FeLoBAL groups compared with the unabsorbed comparison sample groups. The samples are not disjoint, however; for example, the median slope of the $E1 > 0$ FeLoBALQs is only slightly flatter than the unabsorbed objects. The D_{red} parameter shows very similar behavior, indicating that these two parameters are to some extent degenerate; a flatter power law is equivalent to a larger difference from the composite spectrum compiled from the unabsorbed objects.

There are no significant differences in α_{oi} between any of the groups of objects, although the $E1 < 0$ FeLoBALQs show the steepest values of any of the groups. This implies that this group of objects tends to be bluer than other objects. Recalling that α_{oi} measures the optical to NIR slope, a partial explanation for this may be found in the D_{torus} distributions. The FeLoBAL quasars uniformly show a deficit in hot dust emission compared with the unabsorbed quasars as a whole. As discussed in Section 4.2, if reddening is the principal origin of SED differences, the normalization at 1 μm would tend to enhance torus emission in objects inferred to be reddened. The fact that the FeLoBALQs are both reddened and have overall weaker torus emission means that the deficit in hot dust emission is slightly stronger than it appears. The group with the greatest

[10] E.g., https://asaip.psu.edu/articles/beware-the-kolmogorov-smirnov-test/.

Table 2
Parameter Distributions Comparison

Parameter Name	FeLoBALQs versus Comparison						FeLoBALQs	
	All (30/132)		$E1 < 0$ (17/61)		$E1 > 0$ (13/71)		$E1 < 0$ versus $E1 > 0$[a]	
	KS[b]	AD[c]	KS[b]	AD[c]	KS[b]	AD[c]	KS[b]	AD[c]
4500–5500 Å Slope	**0.48/1.3 × 10^{-5}**	**17.6/ < 0.001**	**0.56/2.3 × 10^{-4}**	**9.2/ < 0.001**	**0.48/6.9 × 10^{-3}**	**7.1/ < 0.001**	0.46/0.055	1.9/0.055
α_{oi} (5100 Å–3 μm slope)	0.21/0.20	0.41/0.23	0.29/0.16	0.67/0.17	0.23/0.55	−0.78/ > 0.25	0.28/0.51	−0.06/<0.25
W1−W2	0.11/0.91	−0.86/<0.25	0.26/0.26	0.006/<0.25	0.24/0.46	0.054/<0.25	**0.52/0.025**	**3.8/9.3 × 10^{-3}**
$D_{\rm red}$	**0.37/1.5 × 10^{-3}**	**9.3/ < 0.001**	**0.42/1.1 × 10^{-2}**	**5.4/2.6 × 10^{-3}**	0.39/0.05	**3.7/1.1 × 10^{-2}**	0.18/0.93	−0.82/<0.25
$D_{\rm torus}$	**0.31/1.4 × 10^{-2}**	**4.9/3.7 × 10^{-3}**	**0.42/1.3 × 10^{-2}**	**5.7/2.0 × 10^{-3}**	0.25/0.42	−0.002/<0.25	0.42/0.12	1.4/0.08
W1 Excess Variance	0.14/0.69	−0.80/0.25	0.20/0.59	−0.28/0.25	0.31/0.21	0.64/0.18	0.42/0.11	**2.2/0.04**
W2 Excess Variance	0.23/0.13	0.98/0.13	0.28/0.20	1.6/0.07	0.30/0.21	0.66/0.18	0.47/0.05	**2.4/0.035**
Color Excess Variance	**0.29/0.026**	**2.0/0.048**	0.35/0.056	1.72/0.06	0.35 /0.11	0.88/0.14	**0.57/0.01**	**3.2/0.016**
W1−W2 Correlation Prob.	0.20/0.22	1.03/0.12	0.23/0.41	0.62/0.18	0.24/0.44	0.37 /0.24	0.35/0.25	0.02/<0.25

Notes.
[a] The optical data from the $E < 0$ ($E > 0$) FeLoBALQ subsamples include 17 (13) objects.
[b] The Kolmogorov–Smirnov two-sample test. Each entry has two numbers: the first is the value of the statistic, and the second is the probability that the two samples arise from the same parent sample. Bold type indicates entries that yield $p < 0.05$, i.e., statistically significant.
[c] The Anderson–Darling two-sample test. Each entry has two numbers: the first is the value of the statistic, and the second is the probability that the two samples arise from the same parent sample. We note that the implementation used does not compute a probability larger than 0.25 or smaller than 0.001. Bold type indicates entries that yield $p < 0.05$, i.e., statistically significant.

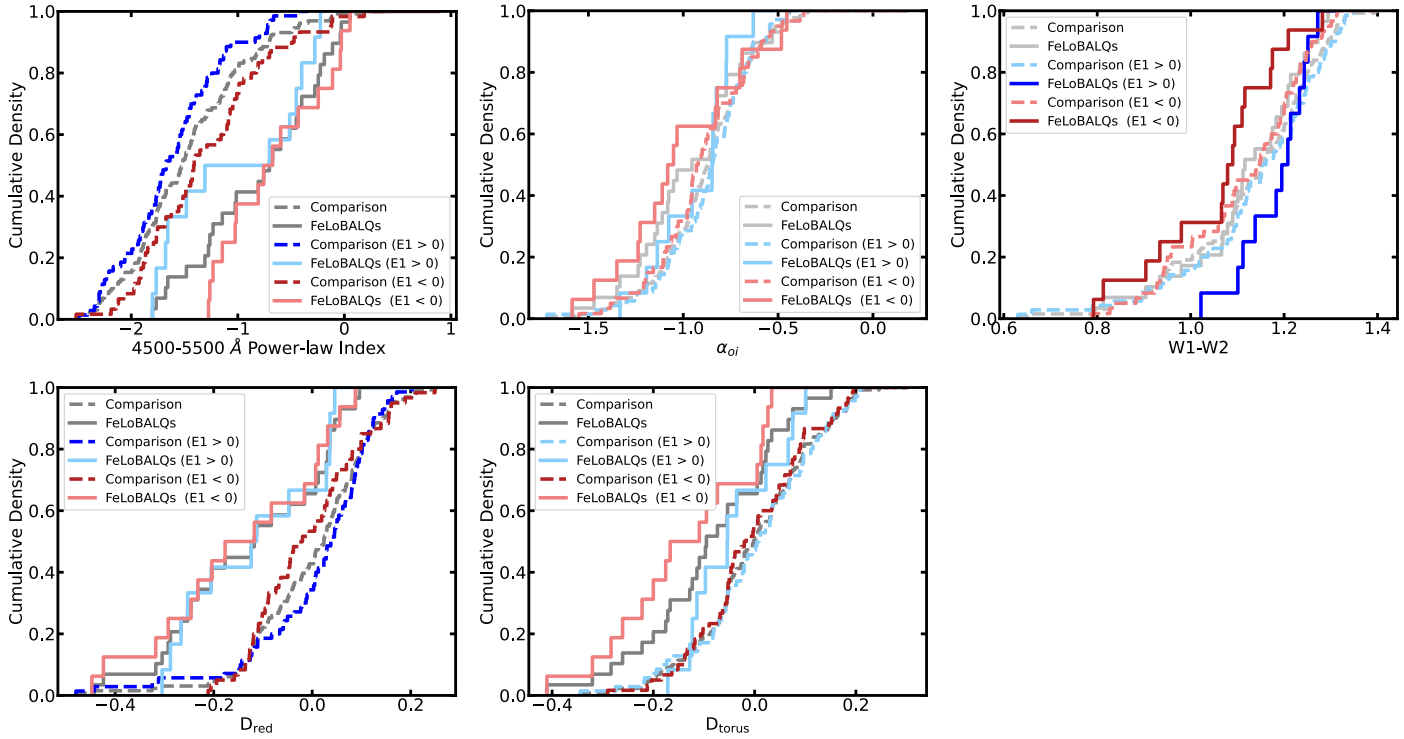

Figure 7. Cumulative distribution plots of the continuum shape parameters. The data are sampled in three ways: the gray lines show the full FeLoBALQ and comparison samples, and the blue (red) lines show the FeLoBALQ and comparison samples for E1 parameter $E1 > 0$ ($E1 < 0$). The Kolmogorov–Smirnov and Anderson–Darling statistics for four different comparisons are given in Table 2. Distributions that are significantly different ($p < 0.05$) are shown in dark red, dark blue, or dark gray, while distributions that are not significantly different are shown in pale colors. The full sample distributions are statistically significantly different for the 4500–5500 Å power-law slope, the reddening excess parameter D_{red}, and the torus excess parameter D_{torus}. The FeLoBALQs partitioned by the E1 parameter are statistically significantly different for only W1−W2.

D_{torus}, i.e., the least evidence for hot dust emission, is that of the $E1 < 0$ FeLoBALQs.

Finally, W1−W2 is consistent between the FeLoBALQs and the unabsorbed comparison sample overall, but there is a significant difference among the $E1 < 0$ and $E1 > 0$ FeLoBAL quasars. Because W1−W2 measures the upturn past one micron toward the torus for these redshifts, this parameter can be interpreted as the prominence of hot dust emission. The $E1 < 0$ objects have lower values of W1−W2, i.e., evidence for a lack of hot dust emission, and thus this result echoes the D_{torus} result.

Overall, these distributions reveal that FeLoBAL quasars have redder optical spectra than unabsorbed objects, and the SEDs suggest that this may in part be due to reddening. In addition, FeLoBAL quasars with $E1 < 0$ ($E1 > 0$) as a group show bluer (redder) infrared spectra, suggesting weaker (stronger) hot dust signatures than the unabsorbed comparison sample quasars.

5.2. WISE Variability Parameters

We found that the FeLoBALQ and unabsorbed comparison sample WISE excess variance distributions are indistinguishable in most cases (Table 2). The most significant distribution difference was found between the $E1$-divided FeLoBALQs. The $E1 > 0$ objects, i.e., the ones with larger L_{bol}/L_{Edd}, were less variable than the $E1 < 0$ objects. In addition, there is a difference in excess variance color whereby the $E1 < 0$ objects varied more in W1 than in W2. The distributions of the three parameters that have statistically significant differences are shown in Figure 8.

The objects in this sample are relatively nearby and have moderate bolometric luminosities. In Section 3.1, we showed that, in most objects, the host-galaxy contamination in the near-infrared band is expected to be negligible. We confirm that result here, because if galaxy contamination were significant, one would expect that the lower-luminosity objects would appear to have a lower-variability amplitude. As shown in Leighly et al. (2022, Figure 8), the $E1 < 0$ objects have a mean inferred bolometric luminosity about 0.5 dex lower than the $E1 > 0$ objects, and yet we found that they are more variable in both W1 and W2. Therefore, while there could be some suppression of variability due to galaxy contamination in some objects, it does not dominate the variability properties.

6. Correlations with the SED and WISE Variability Parameters

We examine the relationships between the five SED and four variability parameters and the emission-line and global parameters presented in Leighly et al. (2022) and the *SimBAL* parameters presented in Choi et al. (2022b). First, we present Spearman-rank correlations, and then we discuss the relationships among various parameters. The results are presented in Figures 9 and 10, which represent the statistical properties of the correlations graphically. We plot the false-alarm probabilities rather than the correlation coefficients, because we compare samples of different sizes.

Parameter uncertainties were propagated through the correlations using a Monte Carlo scheme; see also Leighly et al. (2022). We made 10,000 normally distributed draws of each parameter, where the distribution was stretched to the size

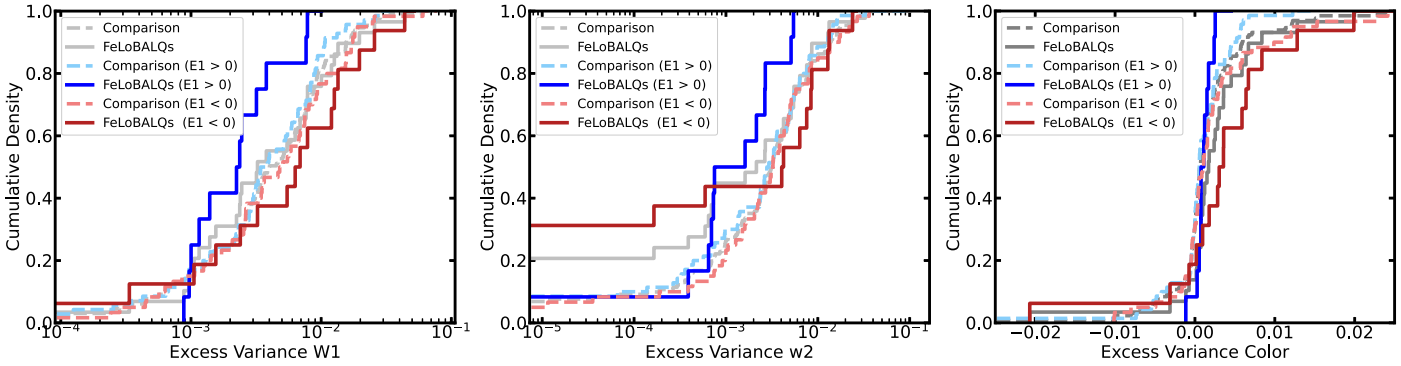

Figure 8. The distributions of three of the four variability parameters, including excess variance for W1 (left) and W2 (center) and the color excess variance (right), where a positive value indicates that W1 varies more than W2. In most cases, distributions of pairs of properties were indistinguishable; the exceptions were the $E < 1$ vs. the $E > 1$ FeLoBALQs for all parameters, and the color excess variance for the FeLoBALQs vs. the comparison objects. The fourth parameter, the correlation p-value between W1 and W2 lightcurves, showed no differences between any of the samples and is not shown.

of the error bar. Asymmetrical errors were accounted for by using a split-normal distribution (i.e., stretching the positive draws according to the positive error, and the negative draws according to the negative error). We chose $p < 0.05$ as our threshold for significance. The overplotted stars in Figures 9 and 10 show the fraction of draws that yield p values greater than our threshold value; these are clearly seen only when accounting for the uncertainty dramatically changes the significance of the correlation. Generally, taking the errors into account did not affect the significance of a correlation, if present.

As discussed in Leighly et al. (2022), correlations among quasar properties associated with the Boroson & Green (1992) Eigenvector 1, here parameterized using the $E1$ parameter, may dominate and potentially obscure other correlations. We would like to determine whether there were correlations independent of the $E1$ parameter. It is also possible that the two classes of FeLoBALQs show different correlation behaviors that would be washed out in the whole-sample correlations. Therefore, we also computed the Spearman-rank correlation coefficient between the parameters divided by $E1 < 0$ and $E1 > 0$ (Figures 9 and 10, middle and right panels).

6.1. Continuum Parameters

6.1.1. The Power-law Index

We first considered the power-law index, which was defined as the slope between 4500 and 5500 Å measured from the continuum portion of the spectroscopy model from Leighly et al. (2022; Figure 3, Table 1). This parameter measures the shape of the optical continuum arising from the accretion disk. This parameter may be intrinsically different from object to object, and it also may be flattened by reddening if present. The distribution analysis (Section 5.1) showed that the power-law index is significantly flatter in FeLoBALQs than in unabsorbed quasars (Figure 7, Table 2), indicating that FeLoBALQs have redder spectra.

Among the unabsorbed comparison objects, the power-law index is strongly anticorrelated with with the Eddington ratio ($p = 9 \times 10^{-5}$; Figures 9, 11); the possible origin of this correlation is discussed in Section 8.1. It is similarly correlated with other parameters related to the Eddington ratio, including $R_{\rm Fe\ II}$, the Spectral Principal Component Analysis (SPCA) E1 coefficient (Leighly et al. 2022), and the $E1$ parameter. Although the power-law index for the FeLoBALQs is not correlated with the Eddington ratio, Figure 11 shows that a rough relationship is present, with the higher-accretion-rate ($E1 > 0$) objects having overall steeper spectra than the lower-accretion-rate ($E1 < 0$) objects. There is a large scatter that may be due to a range of reddening among the FeLoBAL quasars.

6.1.2. $\alpha_{\rm oi}$

We next consider α_{oi}, which is defined as the point-to-point slope between 5100 Å and 3μm (Figure 3, Table 1). This parameter measures the overall steepness of the optical through near-IR spectrum. It may be steep (blue) because the torus contribution is weak. It may be flat (red) because the torus contribution is strong, or because there is significant reddening.

Among the unabsorbed comparison objects, α_{oi} is correlated with the Eddington ratio ($p = 7 \times 10^{-6}$; Figure 11), in the same way as the power-law index is, but with the opposite dependence: objects with steeper (bluer) spectra have lower Eddington ratios. α_{oi} is correlated with the other four SED parameters, as expected, but it is most strongly correlated with $D_{\rm torus}$ ($p = 2 \times 10^{-19}$), suggesting that the α_{oi} is dominated by the range of hot dust emission rather than the range of optical deficits. This correlation may be expected based on the optimal red and blue comparison sample composites shown in Figure 4, where the blue composites show stronger torus emission.

The FeLoBALQs and unabsorbed comparison sample objects show opposite relationships between α_{oi} and the power-law index (Figure 12), where we color code the markers using the optimal red and optimal blue classification discussed in Section 4.2. While the FeLoBALQs show a correlation between these two parameters ($p = 0.002$), the unabsorbed objects show an anticorrelation ($p = 0.016$). Also, the anticorrelation between the Eddington ratio and the power-law index in the unabsorbed objects is mirrored by a correlation with α_{oi}; objects with steep (blue) power-law spectra have flat (red) values of α_{oi} and vice versa.

To help interpret this behavior, we overplotted the inferred α_{oi} and 4500–5500 Å power law from the Krawczyk et al. (2013) composite spectrum subject to SMC reddening with a range of A_V between 0 and 1. This result shows that reddening moves objects upward and to the right (Figure 12). This plot and superimposed arrow shows that the continua of FeLoBALQs are not *simply* reddened versions of unabsorbed quasar continua. Specifically, the unabsorbed quasars show an anticorrelation between power-law index and α_{oi}, stretching from upper left to lower middle. If FeLoBALQs were all

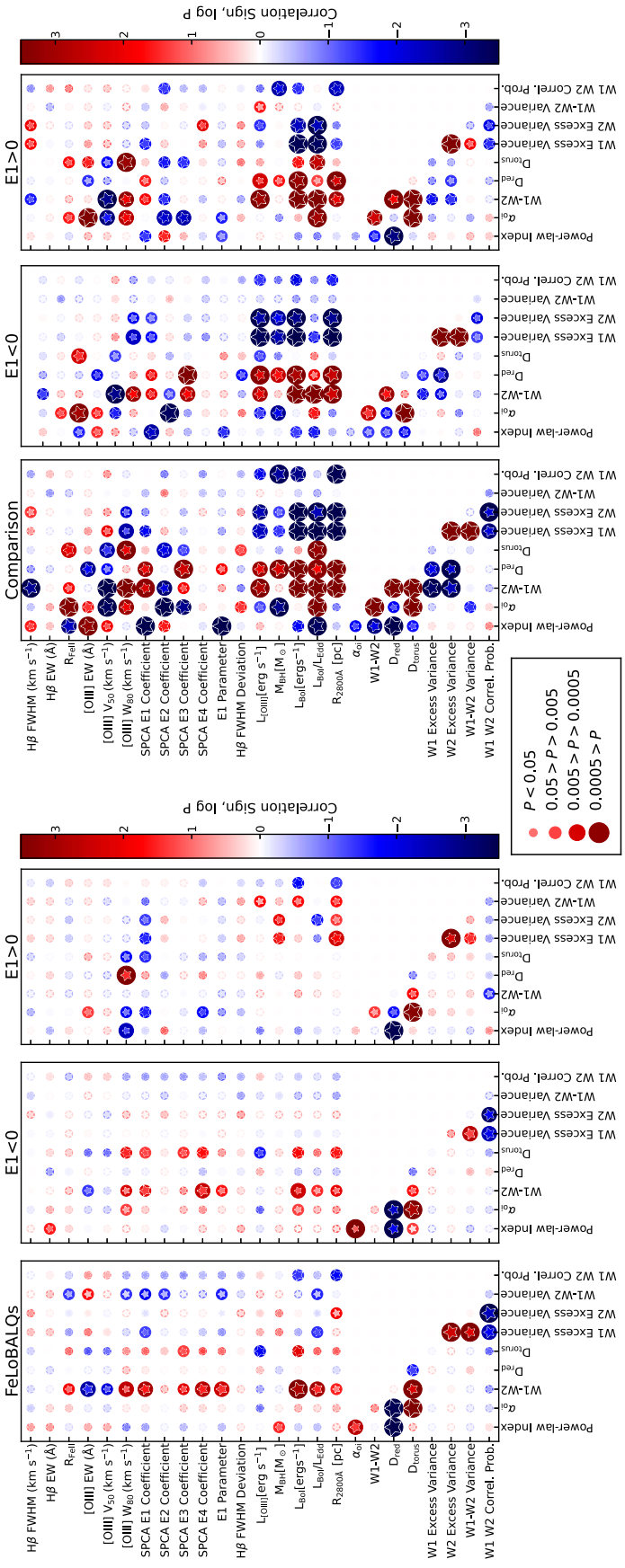

Figure 9. The results of the Spearman rank correlation analysis for the FeLoBAL quasars (left) and the comparison sample (right), and the correlations divided according to the *E*1 parameter. The size and color of each marker indicate the sign and p value of the correlation. Anticorrelations are shown in blue, and correlations are shown in red. The shade of the color of each point indicates the significance of the correlation as a continuous variable, while the discrete sizes of the points characterize a range of p values: $p < 0.05$, $0.05 > p > 0.005$, $0.005 > p > 0.0005$, and $0.0005 > p$. The circular markers show the results for parameter values. The stars show the results for a Monte Carlo scheme to estimate the effects of the errors (see text for details). Many significant correlations are found among the comparison sample properties, in particular with the Eddington ratio, that are not mirrored among the FeLoBALQs.

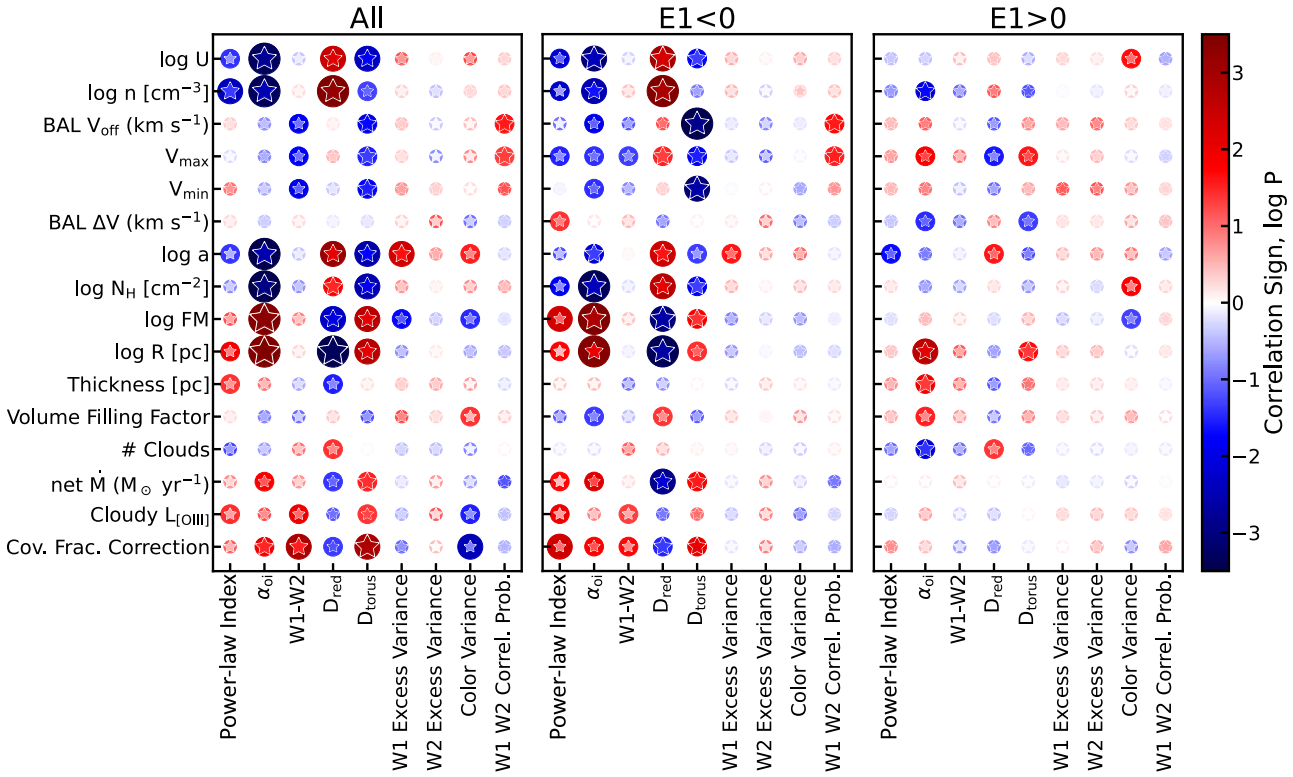

Figure 10. The results of the Spearman rank correlation analysis for five continuum parameters, four variability parameters, and the 16 *SimBAL* parameters. The symbols have the same meaning as in Figure 9. The left plot shows the results for the whole sample, while the middle and right plots show the results for $E1 < 0$ and $E1 > 0$, respectively. Among the continuum parameters, α_{oi}, D_{red}, and D_{torus} are the most strongly correlated with the *SimBAL* parameters. No significant patterns were found among the variability parameters.

reddened versions of the unabsorbed quasars, they would show a similar anticorrelation, with the whole pattern shifted upward and to the right along the arrow. Instead, they show a correlation. In fact, the optimal red FeLoBAL quasars are consistent with being reddened versions of the optimal blue FeLoBAL quasars, since the FeLoBAL correlation in this plot has roughly the same slope as the arrow.

The key to interpreting this plot lies in an examination of the optimal red and blue spectra shown in Figure 4. The unabsorbed quasars differ in the strength of the torus, while reddening is much less important. An interesting feature is that, among the unabsorbed quasars, stronger torus emission is associated with a steeper (bluer) power law, yielding the points in the upper left corner of the plot; the optimal red unabsorbed quasars comprise these points. That is, a very steep (blue) optical power law is associated with a very flat (red) near-infrared spectrum in the unabsorbed objects (Figure 9). That the power law and the prominence of the torus are correlated with the Eddington ratio (Figure 11) might be a clue about the origin of the SED.

FeLoBAL quasars are noticeably absent from the upper-left corner of the plot. This means either that FeLoBAL quasars have intrinsically flatter power-law spectra or that all FeLoBAL quasars have at least some reddening (or both). FeLoBAL quasars that have relatively steeper (bluer) optical spectra (power-law indices less than ~ -0.5) all have weak torus emission (the optimal blue FeLoBALQs), while the FeLOBAL quasars that have flat optical spectra (suggesting more reddening) also have relatively stronger torus emission than the optimal blue FeLoBAL quasars (the optimal red FeLoBALQs). This is the opposite of the behavior observed in the unabsorbed quasars. This behavior supports the idea that, at least for the optimal blue FeLoBAL quasars, the flatter power-law index compared with unabsorbed quasars is, in fact, intrinsic. Otherwise, the optimal red and optimal blue FeLoBAL quasar spectra would have the same torus emission (Figure 4); there should be no reason for strong-torus objects to have more reddening and vice versa. The principal group missing from this plot is that of the reddened unabsorbed quasars, if they exist.

6.1.3. W1−W2

At the low redshifts considered in this paper, W1−W2 measures the rest near-infrared color (Figure 3, Table 1). It quantifies the upturn toward the torus and the presence of hot dust emission. A small value of W1−W2 indicates weak hot dust emission (blue near-infrared continuum), while a large value points to strong hot dust emission and a prominent torus (red near-infrared continuum).

W1−W2 shows some of the stronger correlations with the optical parameters, and unlike the other continuum parameters, correlations among the FeLoBALQs are present. Figure 11 shows the correlations with Eddington ratio; the p values are 1.0×10^{-3} (3.5×10^{-20}) for the FeLoBALQs (unabsorbed objects), respectively.

As noted in Section 3.1, most of our objects have redshifts between 0.8 and 1.0, which means that W1 and W2 describe the flux densities near 1.7–1.86 and 2.3–2.56 μm, respectively. The values fall on the upturn from the 1 μm dust sublimation break toward the torus infrared bump. Thus, the correlations that we find mean that, at low accretion rates, the spectrum lacks this upturn—a property that could be interpreted as a lack

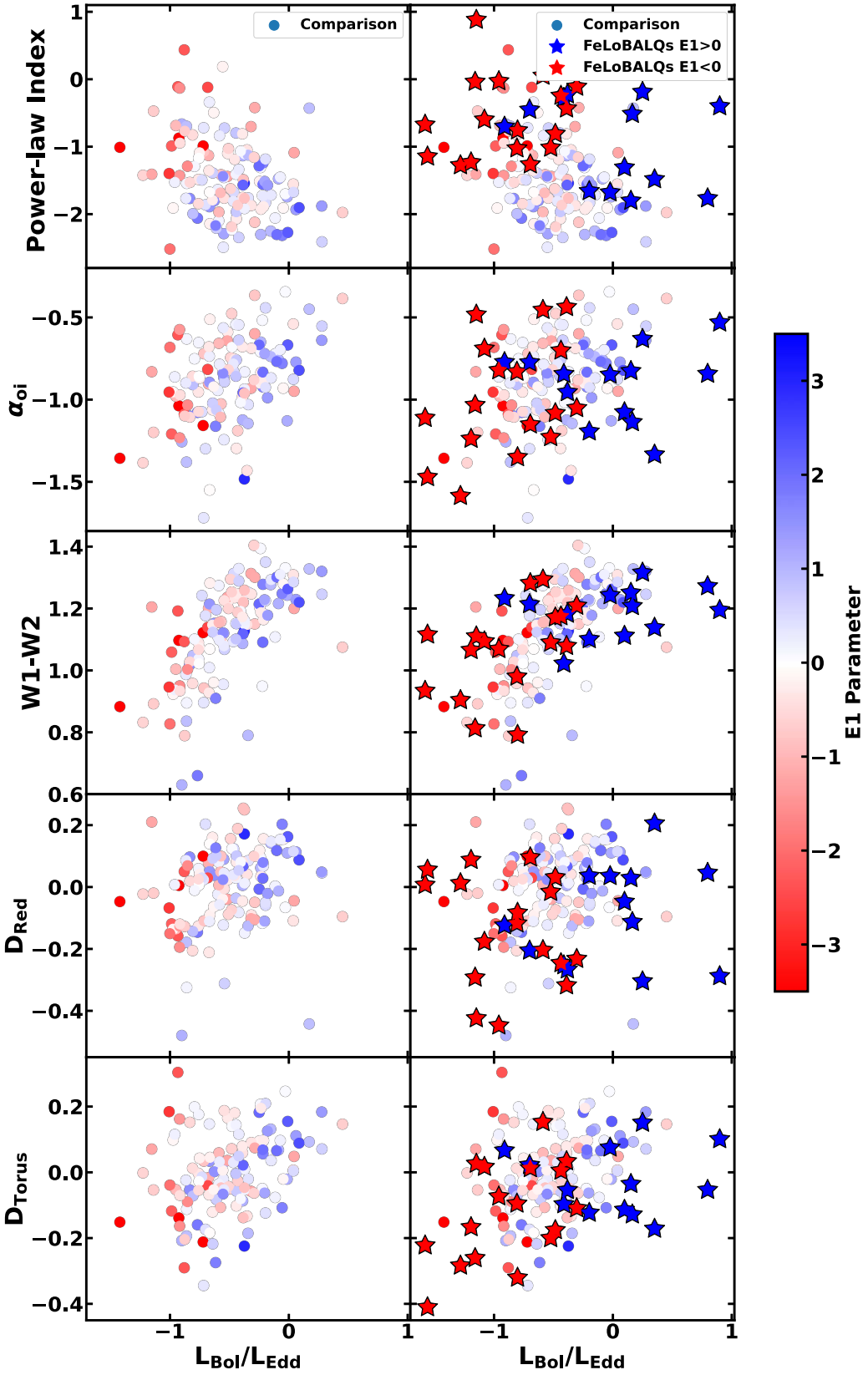

Figure 11. The parameters used to describe the optical–near-IR continuum properties as a function of Eddington ratio. The unabsorbed comparison sample is shown in the left column, and those plus the FeLoBAL quasars are shown in the right column. Significant correlations are seen between all parameters and the Eddington ratio among the unabsorbed quasars (also Figure 9). Among the FeLoBALQs, only the correlation with W1−W2 is significant. The other parameters are more scattered, perhaps as a consequence of different contributions of reddening.

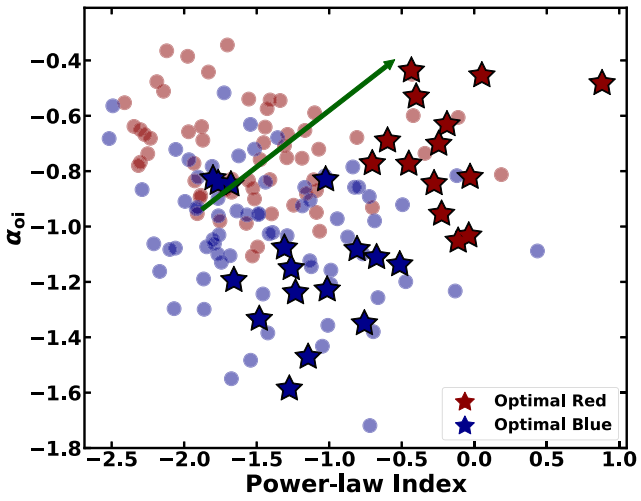

Figure 12. The relationship between α_{oi} and the local power-law index measured under the Hβ/[O III]/Fe II emission. An anticorrelation is found for the unabsorbed objects. The arrow shows $A_V = 1$ for the Krawczyk et al. (2013) composite continuum. If the FeLoBALQs were simply reddened versions of unabsorbed quasars, they would also show similar anticorrelations, but broader and shifted upward and to the right. Instead, they show a correlation.

of hot dust emission. The lack of the hot dust component can be seen in some of the SED photometry plots (Figure 1) and in the optimal blue FeLoBAL composite (Figure 4).

Previous investigations have associated a lack of hot dust emission with a low accretion rate. Objects that lack hot dust are termed HDD, and in the 87 best-studied Palomar–Green quasars, they are linked to relatively lower accretion rates (Lyu et al. 2017). A lack of torus emission in low-accretion-rate objects is supported by a number of other investigations (e.g., Whysong & Antonucci 2004; van der Wolk et al. 2010; Trump et al. 2011; González-Martín et al. 2017; Izumi et al. 2017; Ricci et al. 2017; Temple et al. 2021).

6.1.4. D_{red} and D_{torus}

As discussed in Section 4.2, the $D_{\rm red}$ and $D_{\rm torus}$ parameters were devised to break the degeneracy inherent in α_{oi}. Specifically, α_{oi} may be flat (red) because of reddening in the optical band or strong hot dust emission in the near-infrared band. These parameters were defined relative to the composite created from the unabsorbed objects. $D_{\rm red}$ was defined in the rest optical band; it has a low value if the optical spectrum of an object is flat (red) compared with the composite. $D_{\rm torus}$ was defined in the rest near-IR band; it has a low value when the torus/hot dust emission is weak compared with the composite.

In the correlation analysis, $D_{\rm red}$ and $D_{\rm torus}$ are somewhat redundant with the other parameters; their chief utility is to distinguish the influences on α_{oi}. As noted above, they are not correlated with one another (Figure 5), showing that reddening alone cannot be responsible for the range of continuum properties found. We found that $D_{\rm red}$ and α_{oi} are correlated for the FeLoBALQs but not for the unabsorbed objects, indicating that reddening is more important for shaping the continuum among the FeLoBALQs. In contrast, α_{oi} is correlated with $D_{\rm torus}$ for both samples. This result was also obtained from the optimal red and optimal blue composites shown in Figure 4: the optimal composites from the unabsorbed comparison sample differed longward of 1 μm, indicating variations in the hot dust component of the torus, while the optimal composites of the FeLoBAL quasars also differed shortward of 1 μm, indicating that both reddening and hot dust emission variations are important.

6.2. SimBAL Parameters

Choi et al. (2022a) reported the correlations between the optical emission-line properties and the *SimBAL* parameters. While they found correlations with the outflow velocity and parameters related to the volume-filling factor, no correlations were found with the physical properties of the gas such as the ionization parameter $\log U$, the gas density $\log n$, or the column density $\log N_{\rm H}$. These outflow properties are associated with the location of the gas, i.e., the distance of the absorbing gas from the central engine, $\log R$, which is derived from $\log n$ and $\log U$ using standard, well-established methods based on the theory of photoionized gas as outlined in Section 2.

Surprisingly, we found very strong correlations between the continuum parameters α_{oi}, $D_{\rm red}$, and $D_{\rm torus}$ and the physical properties of the outflowing gas (Figure 10). The strongest correlations are with $\log R$ ($p = 2.2 \times 10^{-6}$, 1.0×10^{-4}, 1.9×10^{-3} for α_{oi}, $D_{\rm red}$, and $D_{\rm torus}$, respectively), arising from an anticorrelation with both $\log U$ and $\log n$. Notably, the α_{oi} correlation persists in both the $E1 < 0$ and $E1 > 0$ subsamples ($p = 4.0 \times 10^{-4}$ and $p = 2.1 \times 10^{-3}$, respectively), so it is not a consequence of accretion rate trends.

The $\alpha_{\rm oi}$ parameter is not easily attributable to a single physical origin. The fact that both $D_{\rm red}$ and $D_{\rm torus}$ are also correlated with the *SimBAL* parameters suggests that both the optical and the infrared regions are participating. A clue may be found in the properties of the loitering outflows. Loitering outflows were identified as a new class of FeLoBAL outflow by Choi et al. (2022b). Despite the location of the outflow near the central engine, they showed very low outflow velocities and relatively narrow absorption lines, yet an overall high absorption opacity due to a large number of high-excitation Fe II lines (the so-called "iron curtain"; Lucy et al. 2018). Leighly et al. (2022) found that they were uniformly low-accretion-rate objects, and Choi et al. (2022a) showed that their outflows had high volume-filling factors approaching one. In the middle panel of Figure 13, the loitering outflow objects that have $0 < \log R < 1$ are notably clustered around $D_{\rm red} = 0$, indicating that they have optical photometry as blue as the comparison composite spectra. At the same time, these objects have low accretion rates and therefore show the lack of hot dust emission indicated by the correlation between accretion rate and W1−W2 noted in Section 6.1.3. In contrast, the objects with outflows located at larger $\log R$ have evidence for a deficit in the optical band ($D_{\rm red} < 0$) and a surplus in the infrared band ($D_{\rm torus} > 0$).

Among the objects with outflows located close to the central engine ($\log R < 1.2$ [pc]), low-accretion-rate objects (8) outnumber the high-accretion-rate ones (4). More high-accretion-rate objects, in particular, high-accretion-rate overlapping trough objects, are found to have outflows located close to the central engine in the Choi et al. (2022b) sample of 50 FeLoBAL quasars (e.g., Choi et al. 2022b, Figure 6); however, their SDSS spectra did not have the Hβ region at the long-wavelength end, principally because their redshifts were larger than 1.0.

Regardless, we interpret these correlations as a general lack of dust signatures near the central engine. Specifically, we suggest that the increase in continuum reddening with outflow

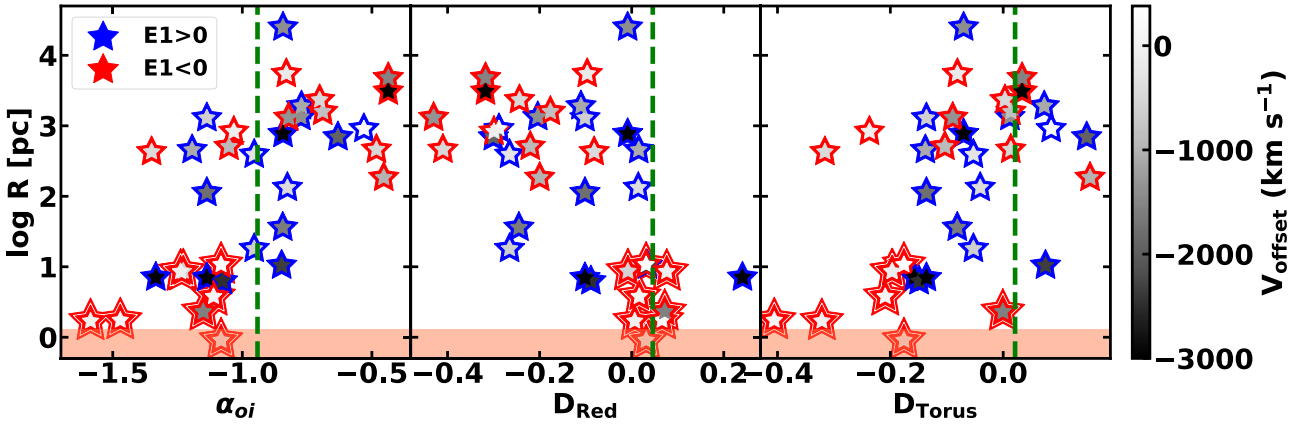

Figure 13. Relationships between the location of the outflow, $\log R$, and several of the continuum properties shaded by the outflow velocity. The vertical dashed lines show the measurement from the Krawczyk et al. (2013) composite continuum for reference. The coral shaded area shows the range of dust sublimation radii, i.e., the inner edge of the torus, among the FeLoBALQs. The double stars show the loitering outflow objects, defined by Choi et al. (2022b) to have $\log R < 1.2$ [pc] and $v_{\rm offset} > -2000$ km s^{-1}. The location of the outflow is a function of the ionization parameter $\log U$ and the density $\log n$ measured using *SimBAL*. Similar correlations are found with the covering fraction parameter $\log a$, the column density $\log N_{\rm H}$, and the force multiplier (Figure 10). Outflows close to the central engine show overall steep (blue) optical/IR continuum spectra (more negative values of α_{oi}), while those located far from the central engine have flat (red) optical/IR continuum spectra (less negative values of α_{oi}).

location suggested by the $\log R/D_{\rm red}$ anticorrelation is evidence for an increased prevalence of SMC-style dust attenuation farther from the central engine; this dust may or may not be directly associated with the outflow. Thus, it may be that intrinsic reddening increases as a function of radius in unabsorbed quasars as well, but because constraining the location of reddening in unabsorbed quasars is difficult, that correlation may be correspondingly difficult to detect.

Similarly, the increase in torus emission with more distant outflow location suggested by the $\log R$–$D_{\rm torus}$ correlation could be evidence for a lack of hot dust at locations close to the central engine, in particular among the low-accretion-rate objects. Examination of the right panel in Figure 13 indicates that low-accretion-rate objects dominate the objects with $D_{\rm torus}$ less than ~ -0.2, and if they were removed, it appears likely that the correlation would not be significant. Indeed, while the p-value for the full correlation is 2×10^{-3}, the p-values are 0.037 and 0.021 for the $E1 < 0$ and $E1 > 0$ objects, respectively, i.e., still significant but not strong.

Finally, we note that the lack of evidence for dust attenuation near the central engine extends only to dust with significant $E(B-V)$, i.e., attenuation in the optical band; the photometry data with wavelengths less than 3000 Å were not used in the spectra fitting, due to the contamination by BALs. At shorter wavelengths, we have found evidence for so-called anomalous reddening (e.g., Choi et al. 2020, Section 4.2) in several objects with outflows close to the central engine. Anomalous reddening is characterized by little attenuation in the optical band, transitioning fairly abruptly to strong attenuation shortward of the near-UV (e.g., Hall et al. 2002; Leighly et al. 2009; Fynbo et al. 2013; Jiang et al. 2013; Meusinger et al. 2016). Such reddening may be produced by a dust distribution dominated by small grains (e.g., Jiang et al. 2013). In particular, FeLoBAL quasars with high-velocity outflows and overlapping troughs frequently showed this type of reddening, and this correspondence may be the origin of the correlation between inferred reddening and outflow velocity found by Choi et al. (2022b).

6.3. Correlations with WISE Variability Parameters

Among the comparison sample objects, the variability amplitude parameters are principally anticorrelated with parameters that depend upon the luminosity and Eddington ratio (Figure 9). This pattern of behavior is commonly found (e.g., Vanden Berk et al. 2004; Wilhite et al. 2008; Kelly et al. 2009; MacLeod & Ivezić 2010; Zuo et al. 2012; Gallastegui-Aizpun & Sarajedini 2014; Simm et al. 2016; Caplar et al. 2017; Sun et al. 2018; Laurenti et al. 2020; Suberlak & Ivezić 2021; De Cicco et al. 2022; Yu et al. 2022). Figure 14 shows the relationship between W1 excess variance and luminosity. The excess variance values for the FeLoBAL quasars are very scattered, and there are no strong correlations with any of the optical or continuum parameters. This phenomenon could point to some alternative parameter dependence, but it is also possible that the stochastic nature of quasar variability is the origin of the scatter and lack of correlation.

The variability parameters for the comparison objects are strongly correlated with the Eddington ratio, $L_{\rm bol}/L_{\rm Edd}$, and with R_{2800}, the characteristic radius for 2800 Å continuum emission (defined in Leighly et al. 2019). Both of these parameters depend on $L_{\rm bol}$. The Eddington ratio dependence is expected to be $L_{\rm bol}^{1/2}$ (i.e., through $L_{\rm bol}$ itself and through the computation of the radius of the broad-line region necessary to compute the black hole mass), and a numerical experiment shows that the R_{2800} dependence should be $L_{\rm bol}^{0.32}$ for a constant black hole mass.

The variability parameters show few correlations with any of the *SimBAL* parameters (Figure 10). In Choi et al. (2022a), we found that the outflow velocity was very strongly correlated with the luminosity, so it might be expected that the commonly known inverse relationship between luminosity and excess variance would spawn a correlation with outflow velocity. None is observed.

We plot color excess variance as a function of the W1 excess variance in Figure 14. Recalling that the color excess variance is defined as the difference between the excess variance of W1 and the excess variance of W2, the excess of points right of the

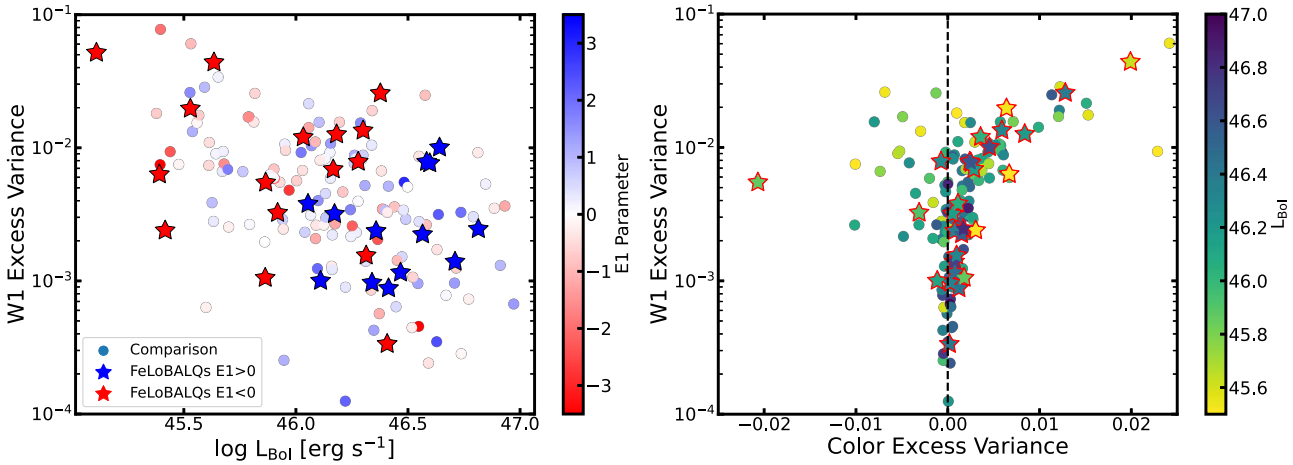

Figure 14. Left: The W1 excess variance is significantly statistically anticorrelated with the bolometric luminosity for the comparison sample (circles). While there is a tendency for the FeLoBAL quasars (stars) to be more variable for lower luminosities, the relationship is very scattered and no significant correlation is present. Right: The W1 excess variance as a function of the difference between the excess variances for W1 and W2 (color excess variance). The FeLoBALQs show stronger variability in W1 than in W2 (positive color excess variance); this behavior is dominated by the low-accretion-rate objects (Figure 8).

color excess variance = 0 line means that objects are more variable at shorter wavelengths. The color excess variance appears more scattered for the comparison sample objects than for the FeLoBALQs. Specifically, 87% of the FeLoBAL quasars have color excess variance greater than zero, while only 69% of the comparison objects show this property. Statistically, this situation constitutes the comparison of two binomial distributions. We can determine whether these distributions are statistically different using the Fisher Exact test.[11] The hypothesis is that the FeLoBAL quasars show greater variance in W1 than in W2, in contrast with the comparison sample, as measured by color variance greater than zero. The p value for this test is 0.037, and therefore there is evidence that the FeLoBAL quasars are more variable in W1 than in W2, in contrast with the comparison objects. Because the color excess variance of the $E1 > 0$ (high-accretion-rate) objects is uniformly close to zero (Figure 8), this difference is driven by the properties of the $E1 < 0$ (low-accretion-rate) objects.

7. A Comparison with LoBAL Quasars

In Leighly et al. (2022), we presented evidence that FeLoBAL quasars have significantly different Hβ/O III/Fe II properties than a luminosity-, redshift-, and S/N-matched sample of unabsorbed quasars. Leighly et al. (2022) found that the distribution of the accretion rate parameter $E1$ was significantly different between the FeLoBAL quasars and the comparison sample. Likewise, the distributions of $R_{\rm Fe\ II}$ and [O III] were also significantly different. The FeLoBAL quasars were characterized by optical emission-line properties that were interpreted as evidence for a low accretion rate (broad Balmer lines, weak Fe II, strong O III, and $E1 < 0$) or a high accretion rate (narrow Balmer lines, strong Fe II, weak O III, and $E1 > 0$).

An obvious next question is whether these trends are shared by other types of broad absorption line quasars, i.e., the LoBAL quasars and the HiBAL quasars. In this paper, we analyzed the sample of LoBAL quasars described in Section 3.3, comparing them with both the FeLoBAL quasars and the comparison sample described in Leighly et al. (2022). Key cumulative distribution functions are shown in Figure 15, and the results of the KS and AD tests are given in Table 3.

The top section of Table 3 shows that the redshift and WISE W1 and W2 magnitude distributions are consistent among the FeLoBAL quasar sample, the unabsorbed quasar sample, and the LoBAL quasar sample. Likewise, the bolometric luminosity distribution is also consistent. This result is not surprising, given the selection criteria used to construct the comparison sample, namely the matching in redshift, S/N, and bolometric luminosity that was estimated using the 3 μm bolometric correction from Gallagher et al. (2007).

Beyond these properties, there is abundant evidence that the LoBAL quasars are neither similar to the FeLoBAL quasars nor to the unabsorbed comparison sample objects (Figure 15). For example, the LoBAL quasars are characterized by stronger Fe II emission than either the FeLoBAL quasars or the comparison sample as whole, yet their $E1$ values show a very small spread and are very close to zero.

To help interpret these results, we also compared the LoBAL properties as a whole to the FeLoBALQ and comparison samples divided by the $E1$ parameter. Those combinations that were consistent with the LoBALQ property distributions are shown in Figure 15. These comparisons show that the LoBAL quasars are more frequently similar to the comparison objects with $E1 > 0$ among properties related to accretion rate, such as Hβ FWHM, $R_{\rm Fe\ II}$, and $L_{\rm bol}/L_{\rm Edd}$. The LoBAL quasars are similar to the FeLoBAL quasars in $D_{\rm red}$, but they are more similar to the unabsorbed objects in power-law index, perhaps indicating that the LoBALs are more subject to reddening that includes attenuation in the rest optical band, rather than being possibly intrinsically flat as are the FeLoBAL quasars.

Our goal for this analysis was to determine whether the LoBAL quasars are more similar to the FeLoBAL quasars or the unabsorbed comparison quasars. These results indicate that they are different from both samples, but suggest that LoBAL quasars are characterized overall by a high accretion rate relative to Eddington. Perhaps they comprise the high-accretion-rate BAL quasars that Boroson (2002) found (see also Turnshek et al. 1997). This superficial analysis also

[11] https://docs.scipy.org/doc/scipy/reference/generated/scipy.stats.fisher_exact.html

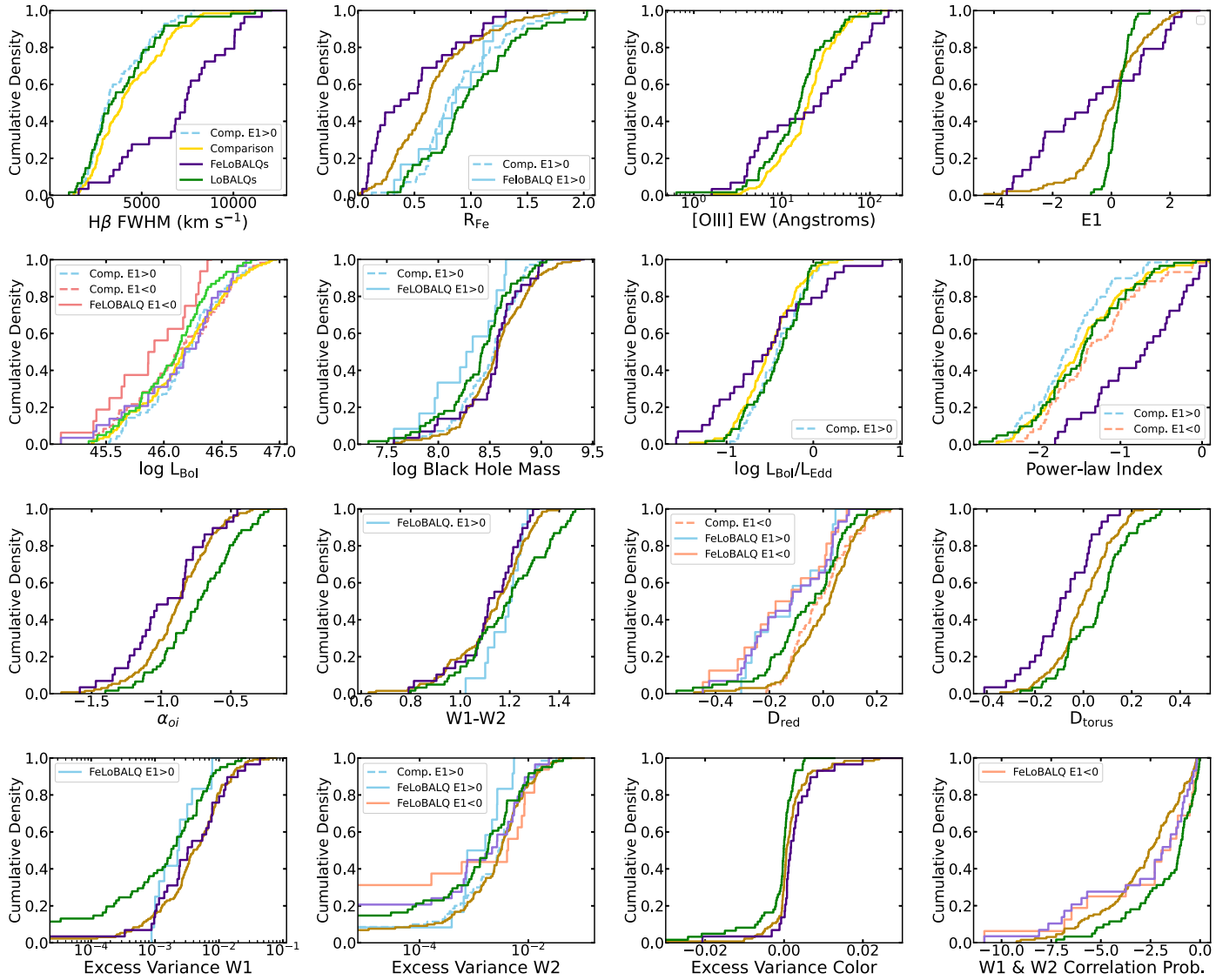

Figure 15. Distribution comparison of optical emission-line, global, continuum, and variability properties between the sample of 62 LoBALQs (green) presented in this paper and the 30 FeLoBALQs (purple) and 132 unabsorbed comparison sample objects (mustard) presented in Leighly et al. (2022). Darker (paler) colors indicate significant (insignificant) statistical differences between the distributions. The legends and lines are included in a panel when an $E1$-partitioned parameter is statistically consistent with the LoBAL parameter distribution. Overall, the subsample that is the most similar to the LoBAL quasars is the $E1 > 0$ comparison sample objects.

suggests that LoBAL quasars may be interesting objects in their own right. For this paper, the most important result is that the accretion properties of the LoBAL quasars are more similar to those of the unabsorbed comparison sample, and they do not show the apparent bimodality that the FeLoBAL quasars do.

It is possible that selection effects influence the results. As stated in Section 3.3, the LoBALQ sample was taken from the DR12 BAL quasar catalog (Pâris et al. 2017). As discussed in Leighly et al. (2022), the FeLoBAL quasars came from a variety of sources, including the literature, the results of our convolutional neural net classifier FeLoNET (Dabbieri et al. 2020), and visual examination. We partially tested the possibility of selection effects by comparing the aforementioned 27 FeLoBALQs found among the $0.75 < z < 1.0$ DR12 BAL objects with the 30 objects discussed here. After removing the three objects in our FeLoBALQ sample that had $z < 0.75$, we found that 12 objects were in both samples. Among those 12, 7 (5) have $E1 > 0$ ($E1 < 0$), so there is no evidence that either accretion state was favored among the FeLoBALs in the DR12Q BAL catalog. In addition, the average $E1$ values of these 12 objects were 1.5 (-1.7) for $E1 > 0$ ($E1 < 0$), i.e., much larger in amplitude than the typical values found for the LoBALQs (Figure 15; -0.22 (0.39) for $E1 < 0$ and $E1 > 0$). Thus, there is no strong evidence that our results are dominated by selection.

8. Discussion

In this paper, we continued our exploration of a sample of 30 low-redshift FeLoBAL quasars. Briefly (see Section 2 for a full review), Choi et al. (2022b) analyzed their outflows using *SimBAL*. Leighly et al. (2022) analyzed their rest-frame optical spectra, focusing in particular on the rich diagnostics available in the Hβ/[O III]/Fe II region of the spectrum. Choi et al. (2022a) combined the results from the first two papers, investigating how the outflow properties depend on accretion rate. This paper focuses on their optical–NIR continuum spectra extracted from archived photometry observations, and their near-infrared variability obtained from the decade-long

Table 3
LoBAL Parameter Distribution Comparison

Parameter Name	FeLoBALQs versus Comparison		LoBALQs versus Comparison		FeLoBALQs versus LoBALQs	
	KS[a]	AD[b]	KS[a]	AD[b]	KS[a]	AD[b]
Redshift	0.14/0.65	−0.03/>0.25	0.13/0.47	0.13/>0.25	0.20/0.35	0.54/0.20
W1 Magnitude	0.08/0.99	−0.82/>0.25	0.19/0.09	**3.0/0.020**	0.25/0.14	**2.09/0.045**
W2 Magnitude	0.10/0.93	−0.74/>0.25	0.16/0.23	1.43/0.08	0.21/0.29	0.93/0.14
$H\beta$ FWHM	**0.56/1.5 × 10^{-7}**	**18.0/<0.001**	0.14/0.32	0.98/0.13	**0.60/2.3 × 10^{-7}**	**15.4/<0.001**
$R_{\rm Fe\ II}$	**0.35/3.6 × 10^{-3}**	**4.5/5.4 × 10^{-3}**	**0.45/3.7 × 10^{-8}**	**17.0/<0.001**	**0.51/2.9 × 10^{-5}**	**14.3/<0.001**
[O III] EW	**0.28/0.034**	**6.5/1.1 × 10^{-3}**	0.18/0.10	1.6/0.07	**0.32/0.022**	**3.7/0.010**
E1 Parameter	**0.34/4.7 × 10^{-3}**	**5.7/1.9 × 10^{-3}**	**0.52/1.6 × 10^{-5}**	**12.7 /<0.001**	**0.35/3.3 × 10^{-5}**	**8.5/<0.001**
SPCA $E1$	**0.33/7.2 × 10^{-3}**	**5.0/3.5 × 10^{-3}**	**0.31/5.0 × 10^{-4}**	**9.0/<0.001**	**0.44/5.3 × 10^{-4}**	**8.0/<0.001**
SPCA $E2$	**0.40/4.7 × 10^{-4}**	**5.1/3.1 × 10^{-3}**	**0.22/0.03**	1.1/0.12	0.22/0.26	0.37/0.24
SPCA $E3$	**0.37/1.5 × 10^{-3}**	**10.3/ < 0.001**	**0.44/7.5 × 10^{-8}**	**17.2/ < 0.001**	0.25/0.12	1.7/0.07
$L_{\rm bol}$	0.11/0.91	−0.72/>0.25	0.15/0.27	0.53 / 0.20	0.21/0.29	0.26/>0.25
$M_{\rm BH}$	0.13/0.79	−0.67/>0.25	**0.23/0.021**	**4.8/4.1 × 10^{-3}**	**0.31/0.029**	**2.1 / 0.044**
$L_{\rm bol}/L_{\rm Edd}$	0.20/0.23	**3.1/0.018**	0.18/0.11	1.74/0.063	0.22/0.22	**3.2/1.7 × 10^{-2}**
4500–5500 Å Slope	**0.48/1.3 × 10^{-5}**	**17.6 / <0.001**	0.10/0.79	−0.77/>0.25	**0.48/9.1 × 10^{-5}**	**12.8/<0.001**
α_{oi} (5100 Å–3 μm slope)	0.21/0.20	0.41/0.23	**0.26/5.2 × 10^{-3}**	**7.8/<0.001**	**0.35 /0.012**	**5.8/1.9 × 10^{-3}**
W1−W2	0.11/0.91	−0.86/>0.25	0.27/0.08	**2.1 / 0.046**	**0.25/7.6 × 10^{-3}**	**5.0/3.5 × 10^{-3}**
$D_{\rm red}$	**0.37/1.5 × 10^{-3}**	**9.3 / <0.001**	0.19/0.069	**4.4/5.6 × 10^{-3}**	0.27 / 0.08	1.32/0.09
$D_{\rm torus}$	**0.31/0.014**	**4.9/3.7 × 10^{-3}**	**0.27/2.8 × 10^{-3}**	**5.0/3.6 × 10^{-3}**	**0.48/9.1 × 10^{-5}**	**10.5 / <0.001**
W1 Excess Variance	0.14/0.69	−0.08/>0.25	**0.30 /** 7.5 × 10^{-4}	**10.2/<0.001**	0.29/0.054	**3.67/0.011**
W2 Excess Variance	0.23/0.13	0.98/0.13	**0.23/0.017**	**2.3/0.035**	0.18/0.49	−0.60/>0.25
Color Excess Variance	**0.29/0.026**	**2.0/0.048**	**0.22/0.027**	**5.4/2.6 × 10^{-3}**	**0.46/2.1 × 10^{-4}**	**9.4/<0.001**
W1 and W2 Correlation Prob.	0.20/0.22	1.03/0.12	**0.36/2.4 × 10^{-5}**	**11.2/<0.001**	0.23/0.18	1.8/0.058

Notes. The FeLoBAL quasar sample includes 30 objects. The unabsorbed comparison sample includes 132 objects. The LoBAL quasar sample includes 62 objects.
[a] The Kolmogorov–Smirnov Two-sample test. Each entry has two numbers: the first is the value of the statistic, and the second is the probability that the two samples arise from the same parent sample. Bold type indicates entries that yield $p < 0.05$.
[b] The Anderson–Darling Two-sample test. Each entry has two numbers: the first is the value of the statistic, and the second is the probability that the two samples arise from the same parent sample. Note that the implementation used does not compute a probably larger than 0.25 or smaller than 0.001. Bold type indicates entries that yield $p < 0.05$.

WISE observations. Finally, rest-frame optical spectra of a new sample of LoBAL quasars were analyzed to determine whether LoBALs are similar to or different from FeLoBALQs in their accretion properties.

8.1. Optical–Infrared Continuum Properties

The fact that the continuum properties in the unabsorbed objects are most significantly correlated with the Eddington ratio and similar parameters (Figure 9, Section 6.1, Figure 11) indicates that much of the variance in the SED shapes is intrinsic to the quasar rather than an extrinsic property such as a reddening (e.g., Davis et al. 2007), or inclination (e.g., Capellupo et al. 2015).

The origin of the optical–UV power-law slope in quasars has long been a mystery. It is believed to be the emission from the accretion disk. However, the accretion disk spectrum should have an $F(\nu) \propto \nu^{1/3}$, corresponding to $F(\lambda) \propto \lambda^{-2.33}$ (e.g., Koratkar & Blaes 1999). This is much steeper (bluer) than observed in most quasars, although a few objects in our sample are nearly as steep (Figure 7). Considerable effort has been devoted to explaining the flatter observed spectra, although these efforts have focused principally on the UV and shorter wavelengths and not the optical wavelengths investigated in this paper. For example, a physical accretion disk is expected to have an atmosphere that will modify the emitted spectrum through atomic processes (e.g., Davis & Laor 2011). Alternatively, an accretion disk wind can also flatten the spectrum (Slone & Netzer 2012; Capellupo et al. 2015). However, one might expect a stronger disk wind in higher-accretion objects, and a correlation between power-law index and Eddington ratio would be predicted, rather than the anticorrelation that we found.

We suggest that the origin of the anticorrelation between the 4500–5500 Å slope parameterized by the power-law index and the Eddington ratio and similar factors originates in the expected changes in the accretion disk structure due to changes in the accretion rate (e.g., Abramowicz & Fragile 2013). As the accretion rate decreases, the accretion disk is expected to switch from an optically thick, geometrically thin standard disk to an ADAF in the inner regions of the quasar central engine, and the radius at which the transition happens is expected to vary with accretion rate. The expected changes in the spectral energy distribution are shown in Mitchell et al. (2023, Figure 2); the spectrum is steeper for higher accretion rates, as we observe. As before, these changes are expected to dominate at short wavelengths, and it is not clear whether the optical band would be affected. However, those models are semi-empirical, and some leeway may be expected.

Turning to the near-infrared region of the spectrum, we examined the W1−W2 color, which at these redshifts measures the upturn toward the torus longward of 1 μm and therefore measures the presence of hot dust emission. We found that, while there was no statistical difference between the

FeLoBALQs and the unabsorbed comparison objects, the color distributions of $E1 < 0$ and $E1 > 0$ FeLoBALs are statistically significantly different (Figure 7, Table 2). W1−W2 was found to be correlated with the Eddington ratio and similar parameters for the unabsorbed comparison sample, and also for the FeLoBALQs (Figure 9). Low values of W1−W2 correspond a weak or absent upturn toward long wavelengths, and quasars exhibiting these properties are called HDD quasars. As noted in the introduction, among the well-studied Palomar–Green quasars, the HDD objects were found to have relatively lower accretion rates (Lyu et al. 2017).

Physically, what might be the origin of the correlation between the accretion rate and the presence of hot dust? We interpret this result in terms of dynamical outflow models of quasars and the expected properties of a quasar as the accretion rate is dialed up or down. The presence of large-scale dynamical outflows in quasars has been proposed by many people. The torus may be the portion of this outflow optically thick enough to both block the view to the central engine and to thermalize incident radiation sufficiently to emit as a near blackbody in the infrared (e.g., Blandford & Payne 1982; Konigl & Kartje 1994; Gallagher et al. 2015). Elitzur & Shlosman (2006) built upon this idea; they suggested that the torus should disappear at low enough accretion rates that the optically thick wind cannot be sustained.

There is a substantial amount of evidence that low-accretion-rate active galactic nuclei lack a torus. For example, Whysong & Antonucci (2004) showed that M87, a radio galaxy that has an ADAF-like spectral energy distribution, does not show thermal infrared emission. Izumi et al. (2017) found that the low-luminosity AGN NGC 1097 lacks a torus. González-Martín et al. (2017) found evidence for the lack of a torus in low-luminosity AGN. Lyu et al. (2017) found that, among the 87 $z < 0.5$ Palomar–Green quasars, objects that are deficient in hot-dust emission are characterized by a low accretion rate. Ricci et al. (2017) found a low fraction of obscured AGN at very low Eddington ratios. Trump et al. (2011) found that the IR torus signature became weaker at low accretion rates in quasars from the COSMOS survey. van der Wolk et al. (2010) found evidence that low-accretion-rate radio galaxies lack a torus.

At low accretion rates, Elitzur & Ho (2009) found evidence that the broad-line region also disappears. These observations are confirmed in other studies. Trump et al. (2011) found that lower-accretion-rate AGNs in the COSMOS survey were unobscured but also lacked a broad-line region. Constantin et al. (2015) found that narrow-line LINERs have weaker emission lines than broad-line LINERs, consistent with the idea that a low accretion rate causes the disappearance of the broad-line component.

These ideas are combined in Elitzur (2008). If we start with a typical AGN with a well-developed broad-line region and torus, and dial the accretion rate down, we should find the infrared emission from the torus disappearing first, since the reprocessing of the incident continuum to thermal emission requires a large column density of gas. The outer broad-line region disappears next, making the Balmer lines appear broader. Ultimately, the broad-line region emission becomes dominated by the double-peaked disk lines seen in broad-line radio galaxies and LINERs (e.g., Storchi-Bergmann et al. 2017). An example is NGC 3147, a candidate true type 2 AGN that apparently lacks broad lines but also suffers no X-ray absorption; an HST observation of that object revealed a disk-line profile in Hα (Bianchi et al. 2019).

8.2. Reddening

Next, we consider the reddening properties. There is evidence for reddening in some but not all FeLoBALQs, recognized in the optimal red and blue composite spectra (Section 4.2, Figure 4) and possibly indicated in the lack of correlations between the continuum parameters and the other parameters (Section 6.1.2, Figure 12). Specifically, in the unabsorbed comparison sample, the power-law index was found to be significantly anticorrelated with the Eddington ratio for the unabsorbed comparison sample (Figure 11). Among the FeLoBAL quasars, no statistically significant correlation was found, but a general impression of anticorrelation with larger scatter toward flatter indices was seen, as well as a deficit of objects with the steepest optical power-law indices (Figures 7 and 12). Our results confirm that it is likely that there is at least a little bit of reddening in the optical band in most FeLoBAL quasars.

More significantly, we found that the presence of strong versus weak optical reddening is not randomly distributed among the FeLoBAL quasars. The *SimBAL* correlations, shown in Figure 13, revealed that objects with more distant outflows show more evidence for reddening than the ones with outflows located close to the central engine.

What is the physical origin of this difference in reddening properties? We speculate that the dust is associated with the outflows in some way. For example, distant outflows may be formed by a shocked ISM (the "cloud-crushing" scenario; Faucher-Giguère et al. 2012); dust is expected to be present in the interstellar medium. Alternatively, dust that causes significant reddening in the optical band—for example, dust with an SMC attenuation curve—may not survive near the central engine, at least in FeLoBAL quasars. Finally, the anomalous reddening that is found in some outflows close to the central engine (Choi et al. 2020, 2022b) may be formed in the outflow itself (Elvis et al. 2002); we speculate that such newly formed dust might have small dust grains, resulting in lack of rest-optical attenuation (e.g., Jiang et al. 2013).

8.3. WISE Variability Properties

We probed the variability properties of the FeLoBALQs and the unabsorbed quasars using the WISE photometry, which samples the near-infrared variability over five years in the rest frame (Section 3.2). We found that, overall, the variability properties were consistent between the FeLoBALQs and unabsorbed quasars, but the variability properties of the $E1 < 0$ and $E1 > 0$ subsamples were significantly different (Section 5.2, Figure 8). The $E1 < 0$ objects were more variable in both the W1 and W2 filters. This may be attributed to the well-known anticorrelation between variability amplitude and luminosity. Also, while the $E1 > 0$ objects showed almost no color variability, the $E1 < 0$ objects showed a greater amplitude of variability in W1 than in W2.

Weak hot dust emission in the low-accretion-rate ($E1 < 0$) FeLoBAL quasars may provide an explanation for their distinctly different variability properties. If the torus emission is weak in the near-IR, the long-wavelength tail of the accretion disk component makes up a larger fraction of the near-IR flux. The accretion disk size scales are much smaller than the torus

size scales, and therefore can be expected to vary with larger amplitude on the sampled time interval, producing the higher-amplitude NIR variability observed in the $E1 < 0$ objects. It is well known that the optical–UV emission in quasars shows larger-amplitude variability at shorter wavelengths (i.e., bluer when brighter; e.g., Vanden Berk et al. 2004; MacLeod & Ivezić 2010; Zuo et al. 2012; Kokubo et al. 2014; Simm et al. 2016), potentially explaining the larger amplitude of variability in W1 compared with W2 among the $E1 < 0$ objects.

Some of the correlations between the variability amplitudes and the optical parameters are suggestive. We found that, in the comparison sample, the WISE excess variance is anticorrelated with the luminosity, as well as other measurements that depend on the luminosity, including the black hole mass, the Eddington ratio, and R_{2800}, the characteristic radius for the 2800 Å continuum emission.

It is well known that lower-luminosity objects have shorter variability timescales than higher-luminosity objects (e.g., Vanden Berk et al. 2004; Wilhite et al. 2008; Kelly et al. 2009; MacLeod & Ivezić 2010; Zuo et al. 2012; Gallastegui-Aizpun & Sarajedini 2014; Simm et al. 2016; Caplar et al. 2017; Sun et al. 2018; Laurenti et al. 2020; Suberlak & Ivezić 2021; De Cicco et al. 2022; Yu et al. 2022). The anticorrelation between the excess variance and R_{2800} that we found may provide an explanation for this behavior through a consideration of interpretations of X-ray variability. Seyfert galaxies are well known to show significant X-ray variability on short timescales, and this variability is one of the principal pieces of evidence that AGNs are powered by accretion onto a central supermassive black hole (e.g., McHardy 1985). It has long been known that the timescale of X-ray variability is anticorrelated with the X-ray luminosity (e.g., Barr & Mushotzky 1986; Green et al. 1993; Lawrence & Papadakis 1993; Nandra et al. 1997), a fact that has been interpreted as an indication that lower-luminosity objects have smaller emission regions, i.e., black hole masses. For example, using *ASCA* data, Leighly (1999) found that narrow-line Seyfert 1 galaxies (NLS1s) showed systematically larger excess variances than broad-line objects of the same X-ray luminosity. The larger excess variance implies a smaller emission region size for the $1/f$ noise typical of X-ray variability in Seyfert galaxies. Hence, Leighly (1999) concluded that NLS1s have smaller black hole masses for the same accretion rate than do broad-line objects, i.e., they have a higher Eddington ratio. This result formed a cornerstone for our understanding of NLS1s.

It therefore seems possible that the excess variance anticorrelation with R_{2800} is simply an anticorrelation with the size of the emission region. Since R_{2800} is correlated with the luminosity (Figure 12 in Leighly et al. 2022), the origin of the commonly observed inverse correlation between variability amplitude and luminosity may be simply be a consequence of a correlation between luminosity and emission-region size.

8.4. The LoBAL Quasar Sample

We compared the rest-frame optical emission-line properties of a sample of LoBAL quasars with similar redshifts and luminosities with the FeLoBAL quasars and the unabsorbed comparison sample (Section 3.3). We also compared the global, continuum, and WISE variability parameters. Our goal was to determine whether the LoBAL quasars split into two groups like the FeLoBAL quasars, or whether the FeLoBAL quasars are a special group among BAL quasars. We found that many but not all of the properties are consistent with the unabsorbed comparison sample (Figure 15, Table 3). The LoBAL quasars do not split into two groups in $E1$, Eddington ratio, or similar parameters. We conclude that FeLoBAL quasars are a special class of object, distinct from both unabsorbed quasars and other broad absorption line quasars.

As discussed in Section 7, it is possible that the LoBAL sample is affected by selection effects. Creating a selection-free sample of quasars is well known to be difficult, and this difficulty is compounded if objects are reddened and their emission lines absorbed. With Gaia, astrometric selection provides a promising method that could yield a quasar sample that, while not completely selection free, at least has simple selection criteria that can be modeled. Krogager et al. (2023) describes the 4MOST-Gaia Purely Astrometric Quasar Survey (4G-PAQS), a project that will carry out the first large-scale completely color-independent quasar survey using a sample selected solely based on astrometry from Gaia. It is expected to obtain a sample of 100,000 quasars over the five years of the 4MOST project—sufficient to obtain a substantial sample of LoBAL and FeLoBAL quasars.

The analysis presented in Section 7 does not support the possibility that the differences between FeLoBALQs and LoBALQs are driven by selection effects. Therefore, until the 4G-PAQS sample has been analyzed, we conclude that FeLoBAL quasars are both different from unabsorbed quasars, as shown in Leighly et al. (2022), and different from other BAL quasars.

8.5. The Accretion Properties of FeLoBAL Quasars

In Leighly et al. (2022), we showed that FeLoBAL quasars are significantly different in their accretion properties than the unabsorbed comparison sample. We established that, while a luminosity-, redshift-, and S/N-matched sample of unabsorbed quasars is characterized by a single peaked distribution in accretion properties, the FeLoBAL quasars more naturally divide into high-accretion-rate and low-accretion-rate groups.

In Choi et al. (2022a) and in this paper, we divided the FeLoBAL quasars into two groups based on the $E1$ parameter, and bent to the task of characterizing the differences between the two groups. These differences are summarized in Figure 16.

Using the ideas discussed in those papers and above in Section 8.1, we now present explanations for the origins of the two populations of FeLoBAL quasars, followed by a description of how FeLoBAL quasars fit into the quasar general population.

8.5.1. The Origin of FeLoBALQs with $E1 < 0$

We have clearly established that the $E1 < 0$ FeLoBAL quasars are low-accretion-rate objects. As discussed in Leighly et al. (2022), the presence of such objects among a sample of BAL quasars is not necessarily expected. Boroson (2002) suggested that BAL quasars have high accretion rates and high Eddington ratios. All of the $E1 < 0$ objects defy that conjecture; they fall among the radio-loud objects in the Boroson (2002) scenario (Leighly et al. 2022, Figure 14). However, their radio properties have not been systematically investigated yet.

Fe II absorption is not unknown in low-accretion-rate objects. It has been documented in Arp 102B, the prototypical double-peaked emission line AGN (Halpern et al. 1996;

Parameter	E1>0	E1<0	Reference
Optical Emission-line Properties	Narrow Hβ, weak[OIII], strong FeII	Broad Hβ, strong [OIII], weak FeII	Paper II
Luminosity	High luminosity	Low luminosity	Paper II
Accretion rate	High Eddington Ratio	Low Eddington Ratio	Paper II
Outflow velocity	High outflow velocities at small radii	Low outflow velocities at small radii (loitering outflows)	Paper III
Volume-filling Factor	Low; many "clouds" needed to occult continuum emission region	High; few "clouds" needed to occult continuum emission region	Paper III
Optical Power-law Index	Marginally steeper (bluer)	Marginally flatter (redder)	This paper
W1-W2	Flatter (brighter hot dust)	Steeper (fainter hot dust)	This paper
Near-IR Variability	Less variable (larger emission region?)	More variable (smaller emission region?)	This paper

Figure 16. A summary of the observed differences in emission-line, continuum, variability, and outflow properties divided by accretion rate parameter $E1$ for the two FeLoBALQ classes.

Eracleous et al. 2003). The HST spectrum of this object (Figure 1 in Halpern et al. 1996) clearly shows high-excitation Fe II lines characteristic of a relatively high-density absorber. Fe II absorption has been found in a few other broad-line radio galaxies (Eracleous 2002), as well as in LINERs and other low-accretion-rate objects (Shields et al. 2002; Sabra et al. 2003). We suggest that our $E1 < 0$ subsample are drawn from the higher-accretion-rate portion of the same parent sample for the broad-line radio galaxies and LINER objects reported in the literature to exhibit Fe II absorption.

The key to understanding Fe II absorption in low-accretion-rate objects may lie in the expected and observed properties of the quasar central engine as the accretion rate is dialed down. We propose that the Fe II absorption in the compact $E1 < 0$ objects (the loitering outflows) marks a stage in this scenario, as follows. The reprocessed continuum emission observed at infrared wavelengths that characterizes objects with moderate and high accretion rates requires the torus to be very optically thick. Elitzur (2008) presented a scheme for the evolution of an AGN as the accretion rate decreases (see Figure 12 in that publication). Specifically, as the accretion rate is dialed down, there is not enough energy to sustain the wind that is the torus, and the torus disappears.

We speculate that a decreasing accretion rate does not manifest as a sudden disappearance of the torus; rather, it may become optically thinner by degrees. At first, the dust optical depth drops to the point that it is no longer optically thick enough to reprocess continuum light into the near-infrared; the near- to mid-IR torus emission would disappear, as we observe. At some point, the remaining column density in the torus may become low enough that the dust can be sublimated and the remaining gas photoionized. If the column density is still substantial enough to include the hydrogen ionization front (Strömgren sphere) in the photoionized slab, Fe^{+} ions may be present, creating the signature of an FeLoBAL. At this point, the torus wind motion may be dominated by rotation rather than outflow, explaining the low velocities characteristic of the $E1 < 0$ FeLoBAL quasars and distinct from the $E1 > 0$ FeLoBALQs with torus-scale outflows (Figure 4, Choi et al. 2022a). Likewise, the remaining torus gas may be mostly uniformly distributed, explaining the large filling fraction also characteristic of $E1 < 0$ FeLoBALQs (Figure 8, Choi et al. 2022a). Finally, ablation of the outer broad-line region may explain the systematically broader Hβ FWHM observed among the $E1 < 0$ objects (Leighly et al. 2022, Section 3.4.1, Figure 13).

8.5.2. *The Origin of FeLoBALQs with* $E1 > 0$

We have clearly established that the $E1 > 0$ FeLoBAL quasars are high-accretion-rate objects. Boroson (2002) suggested that all BAL quasars have high accretion rates and high Eddington ratios, and the $E1 > 0$ FeLoBAL quasars conform to that expectation (Leighly et al. 2022, Figure 14).

To understand the $E1 > 0$ FeLoBALQs, we turn to their Hβ FWHM properties. Leighly et al. (2022) found Hβ FWHM to be systematically broader for the FeLoBALQs compared with the unabsorbed quasars (Section 3.4.1, Figure 13 of that paper). As discussed in that paper, there are two explanations for this result: (1) $E1 > 0$ FeLoBAL quasars are ordinary quasars viewed at a large angle from the normal to the system symmetry axis; or (2) $E1 > 0$ FeLoBAL quasars lack emission in the core of the line, making the line appear broader.

The evidence that supports the larger inclination angle principally comes from studies of LoBAL quasars, originally thought to be a plausible parent sample of FeLoBALQs (although it has been shown in this paper to be different). LoBAL quasars are more likely to be highly polarized than HiBAL quasars (e.g., DiPompeo et al. 2013), suggesting suppression of the continuum along the direct line of sight and allowing the polarized light from axial or high-latitude scattered emission to be detected (e.g., Wills et al. 1992; Leighly et al. 1997). LoBAL quasars can be red or can be found preferentially in samples of red quasars (e.g., Urrutia et al. 2009), and they are generally extremely X-ray weak (e.g.,

Green et al. 2001; Morabito et al. 2011), suggesting a line of sight to the central engine through obscuration (although the discovery of radio-loud BAL quasars casts some doubt on the general applicability of this scenario; see, e.g., DiPompeo et al. 2013). Thus, the broader Hβ lines found in our sample may be explained if they are viewed at a larger angle with respect to the normal. Leighly et al. (2022) showed that, if the average inclination angle to unabsorbed quasars is 30° to the normal (e.g., Shen & Ho 2014), an inclination of 48° is required for the FeLoBAL quasars.

However, there are several $E1 > 0$ FeLoBAL quasars that have peculiar properties that cannot be easily explained by a large inclination angle. We propose that the lines in these objects are broad because there is less emission from slower-moving gas, i.e., diminished emission in the core of the line profile. This interpretation is consistent with the $E1 > 0$ composite spectrum shown (Leighly et al. 2022, Figure 9), which indicates that the Fe II emission is as strong as in the average composite spectrum but the Hβ line is weaker yet no less broad at the base. It may also be consistent with the scenario proposed by Storchi-Bergmann et al. (2017), who suggested that a disk line is a common component in the spectra of Seyfert 1 galaxies that is not generally recognized because of the presence of additional lower-velocity non-disk clouds (see also Bon et al. 2009). The additional lower-velocity component may be comparable to the so-called intermediate-line region (e.g., Brotherton et al. 1994). We suggest that, in some of the $E1 > 0$ objects, the intermediate-line region emission is weak, producing a broader Hβ line with lower equivalent width, as well as a higher $R_{\rm Fe\,II}$ ratio.

Figure 17 shows the Hβ/[O III] region of the spectrum from three of our more luminous $E1 > 0$ FeLoBAL quasars. The Hβ line shows a stubby and boxy profile, and comparison with the unabsorbed composite spectrum suggests that they are missing the low-velocity gas.

In Section 3.4, we modeled the Hα line from SDSS J144800.15+404311.7. We found that it was adequately modeled using a disk line with an outer radius of 9500 gravitational radii. Leighly et al. (2022) estimated a log black hole mass of 8.55, corresponding to an outer radius equal to 0.16 parsec. In contrast, single-epoch reverberation estimation predicts an Hβ reverberation radius of ∼0.3 parsec. Thus, the model fit predicts that the emission line region has a significantly smaller size than expected, i.e., intermediate-line emission gas is missing, leading to overall broader lines.

Why would the intermediate-line region be missing in some objects? A clue to this may come from the behavior of the Hβ deviation parameter discussed in Section 3.4.1 of Leighly et al. (2022). The Hβ deviation parameter was defined to measure the difference between Hβ FWHM measurements and the average values of the unabsorbed comparison sample as a function of $R_{\rm Fe\,II}$. Leighly et al. (2022) showed that the Hβ deviation parameter is significantly anticorrelated with the maximum outflow velocity and correlated with the velocity widths: thus, objects with powerful outflows have broader Hβ lines for their $R_{\rm Fe\,II}$ value. The lower-velocity gas producing the core of the emission line lies farther from the central engine than the higher-velocity gas, and it may be that the location of this gas is close to the torus. We speculate that there is a torus/wind connection *also* among the $E1 > 0$ objects; perhaps the outer broad-line region where the line core would be emitted is disrupted due to the outflow. The nature of this connection is not known, and is quite possibly indirect, as the relationship again appears stochastic rather than deterministic, since we lack evidence for a disk line in any other of our $E1 > 0$ objects. However, the low-redshift range of our sample means that, while we are rather more sensitive to low-accretion-rate objects, we are less sensitive to very high-accretion-rate objects, since those objects are rare and a large volume needs to be surveyed. It may be that a higher-redshift sample will reveal more FeLoBAL quasars with disk-line profile Balmer lines. We are currently making observations of a sample of higher-redshift FeLoBAL quasars, and we have not yet found any with such an extreme Hα profile.

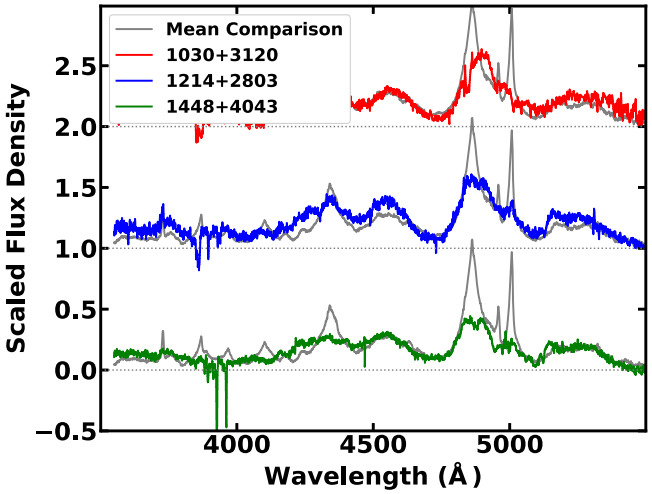

Figure 17. Unusual Hβ line profiles among luminous $E1 > 0$ FeLoBALQs. The boxy shape and the Hβ equivalent width being lower than in the comparison composite suggest that the broad-line region lacks low-velocity gas.

8.6. Speculations on an Evolutionary Scenario

The results presented in Leighly et al. (2022) and this paper link the properties of FeLoBAL quasars directly to differences in accretion rate. As shown by Leighly et al. (2022), $E1 > 0$ FeLoBAL quasars have high accretion rates, $E1 < 0$ FeLoBAL quasars have low accretion rates, and unabsorbed quasars have intermediate accretion rates. If a quasar episode is characterized by an initially large accretion rate, perhaps originating from a merger, followed by a decreasing accretion rate as the fuel supply runs low, we can speculate that the direct link to accretion rate that we have uncovered implies an indirect link to quasar evolution. We explore this scenario in this section.

Sanders et al. (1988a, 1988b) proposed an evolutionary link between infrared-luminous galaxies and quasars that follows a merger event. Infrared galaxies at low redshift often show merger signatures. A merger may allow gas to be funneled to the nucleus, captured by the black hole, and fuel the quasar during its lifetime. Shrouded by a thick layer of gas and dust, the energy provided by the black hole is reprocessed into the infrared, creating a warm ultraluminous galaxy. Eventually, the accreting black hole produces sufficient energy to shrug off its cloak of gas and dust and a quasar is born. Finally, the fuel source decreases, producing a dormant early-type galaxy (e.g., Klindt et al. 2019).

LoBAL quasars have been proposed to play a role in this evolutionary scenario. At low redshifts, LoBAL and FeLoBAL quasars are more frequently found among infrared-selected

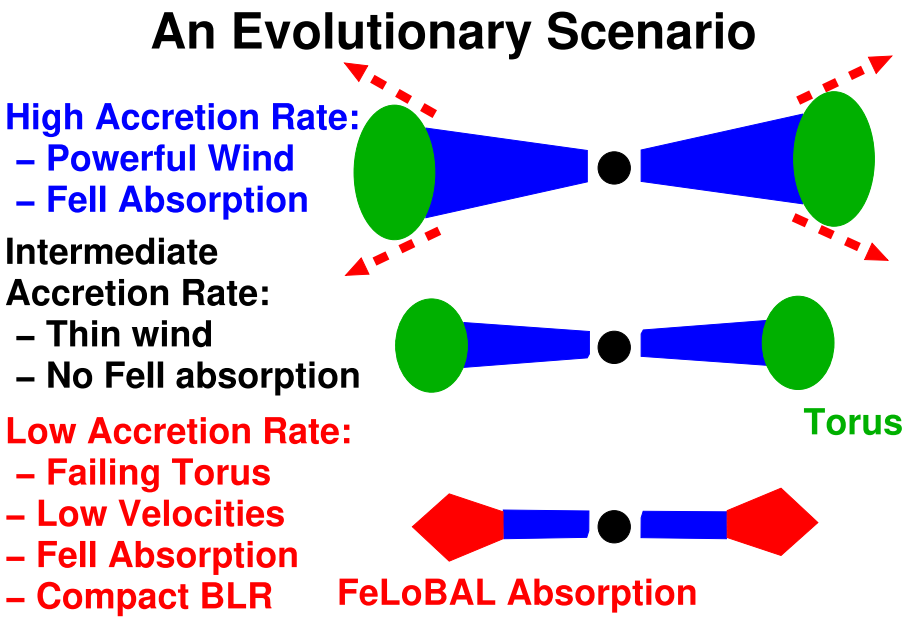

Figure 18. A proposed evolutionary sequence for FeLoBAL quasars. Black denotes the black hole, blue shows the accretion disk, green illustrates the infrared-emitting torus, and red displays the region producing Fe^{+} ions. Top: the $E1 > 0$ objects are characterized by a high accretion rate relative to the Eddington value. They emit sufficient energy to accelerate a thick wind from the vicinity of the torus or throughout the central engine. Middle: the typical quasar may have a BAL wind, but it is generally not thick enough to include Fe^{+} ions. Bottom: the low-accretion-rate quasar loses its ability to sustain an optically thick torus wind (Elitzur & Shlosman 2006), yet retains sufficient gas for Fe^{+} ions to be present in the torus remnant.

quasars (Low et al. 1989; Boroson et al. 1991) and red quasars (Becker et al. 1997; Dai et al. 2008; Urrutia et al. 2009). Many such reddened objects are luminous (Dai et al. 2012) and have high accretion rates (Urrutia et al. 2012), and there is evidence they are in a blow-out phase (Glikman 2017). The reddening and high accretion rates suggest that the LoBAL and FeLoBAL stages should occur after the ULIRG stage and before the bare quasar stage. These interpretations seem plausible; because the BAL outflow in an FeLoBAL quasar must include the hydrogen ionization front to show absorption from Fe^{+}, the ratio of column density to radiative-driving flux density must be high, and so significant energy must be present to accelerate the gas. A high accretion rate provides an environment in which these conditions may be met.

In this sequence of papers, we learned that not all FeLoBAL quasars have high accretion rates. Instead, we found a population of objects that have low accretion rates. This set of objects is clearly disjoint from the high-accretion-rate objects; the only property that they share is the presence of Fe^{+} ions in the line of sight. As outlined in Section 8.5.1, we propose that, in these objects, and especially in the subclass of loitering outflow objects, the Fe II absorption arises from the disintegrating torus.

These results suggest that the FeLoBAL quasar phase may occur at two points in a quasar's evolution: between the ULIRG and bare quasar stage, while the object is accreting rapidly, and between the bare quasar stage and the slide into senescence as the quasar runs out of fuel and the black hole becomes quiescent. This evolutionary scenario is illustrated in Figure 18.

Why was the low-accretion-rate branch of the FeLoBAL quasars not recognized earlier? There are several ways that our experiment differs from the previous ones. First, our convolutional neural net classifier discovered a substantial number of previously missed FeLoBAL quasars in the SDSS quasar catalog. Second, we were able to compile a moderate-sized sample with uniform properties (e.g., luminosity) by using the broad bandpass available on the SDSS. Previous experiments required followup observations in the near-infrared (e.g., Schulze et al. 2017, 2018), and so the samples were smaller and the observational properties less uniform.

Another reason that low-accretion-rate objects are expected to be hard to find is because they are less luminous and therefore more likely to drop out of flux-limited samples (Jester et al. 2005; Hopkins et al. 2009). The $z < 1$ selection of our sample combined with the sensitivity of the SDSS and BOSS projects apparently fortuitously probed the right region of parameter space to yield about 17 $E1 > 0$ and 13 $E1 < 0$ objects. In addition, 11 of our 30 objects are newly identified FeLoBALQs (Section 2.1, Leighly et al. 2022). The mean and median bolometric luminosities of the previously discovered objects are almost 0.4 dex higher than the mean and median bolometric luminosities of the 11 new objects, and 72% of the newly discovered objects are $E1 < 0$ objects.

What, then, can we expect from the 4G-PAQS survey briefly described in Section 8.4? The selection cutoff in that survey is Gaia $G < 20.5$ (Krogager et al. 2023). It turns out that 27 of our 30 objects are brighter than that limit, so we should observe sufficiently varied accretion rates among the new sample objects. Not surprisingly, though, all three of the objects in our current sample with $G > 20.5$ are low-accretion-rate objects.

9. Summary, Conclusions, and Future Work

This is the fourth in a series of papers quantifying the outflow, accretion, and variability properties of a sample of low-redshift FeLoBAL quasars. The first three papers are summarized in Section 2. In this paper, we investigated the optical to near-IR continuum properties and the WISE variability properties. We also performed an analysis of a sample of LoBAL quasars to determine whether the unusual set

of accretion properties exhibited by FeLoBALQs were shared with their lower outflow column density cousins, and presented analysis of a near-IR spectrum of one of our objects. We summarize the principal results below.

1. Using the rest-frame optical to near-infrared continuum properties (Sections 3.1 and 4.2) extracted from photometry measurements of the 30 FeLoBAL quasars and 132 unabsorbed quasars from a matched sample introduced in Choi et al. (2022b) and Leighly et al. (2022), we found significant distribution differences (Section 5.1) and correlations (Section 6.1) among the high- and low-accretion rate FeLoBAL quasars, as well as the unabsorbed quasars. Among the most statistically significant results was the discovery that the optical power-law slope is overall steeper in the unabsorbed objects compared with the FeLoBAL quasars, likely pointing to intrinsically flat spectra and/or at least a small amount of reddening in most FeLoBAL quasars. We found that the low-accretion-rate FeLoBAL quasars lacked evidence for the near-IR upturn that indicates the presence of hot dust (Figure 7), a result that is explained by their low accretion rates (Section 8.1). We found that the continuum parameters were most strongly correlated with the Eddington ratio in the unabsorbed objects, arguing for an intrinsic origin, but these patterns were muted among the FeLoBAL quasars, likely a consequence of a range of reddening (Figures 11, 12).
2. We examined correlations between the continuum shape parameters and the *SimBAL* parameters compiled in Choi et al. (2022b; Section 6.2). We found evidence for a lack of dust close to the central engine in the FeLoBAL quasars that is manifested by a lack of reddening in all objects, and weak hot dust emission in the low-accretion-rate FeLobALQs. We attribute the distribution differences and correlations to structural differences in the central engine driven by accretion rate (Section 8.1), combined with a range of reddening.
3. We investigated the near-infrared variability of the samples using WISE and NEOWISE data (Section 3.2). After correcting a systematic underestimation in the photometry uncertainty (Appendix), we found that, while the variability amplitude did not differ between the FeLoBALQs and the comparison sample, the low-accretion-rate FeLoBALQs showed a higher amplitude of variability than the high-accretion-rate FeLOBALQs (Section 5.2). We examined correlations between the variability amplitude parameters and the emission line and global properties compiled in Leighly et al. (2022). We recovered the typical anticorrelation between variability amplitude and luminosity, and found that evidence that W1 shows stronger variability than W2 in FeLoBALQs but not in the comparison sample objects (Section 6.3). We found evidence for an anticorrelation between the variability amplitude and R_{2800}, the predicted size of the continuum emission region at 2800 Å. We suggest that the commonly found anticorrelation between variability amplitude and luminosity is a consequence of a correlation between luminosity and emission region size (Section 8.3).
4. By analyzing the rest-frame optical spectra, the photometry, and the WISE variability of a redshift-matched sample of LoBAL quasars (Section 3.3), we concluded that FeLoBAL quasars, found to be different from unabsorbed objects, are also different from other types of BAL quasars, and therefore they are truly special objects (Section 8.4). Specifically, the LoBAL quasars were more similar to the unabsorbed comparison sample than to the FeLoBALQs in properties related to accretion rate (Section 7).
5. In Sections 8.5.1 and 8.5.2, we presented our explanations for FeLoBAL absorption in the low-accretion-rate and high-accretion-rate FeLoBAL quasars, with particular focus on the objects with outflows found by Choi et al. (2022b) to be located close to the active nucleus.

Based on the overwhelming evidence of the segregation of FeLoBAL quasars into two groups, as well as the evidence that these two groups represent high and low accretion rates (Leighly et al. 2022), we presented an evolutionary scenario in Section 8.6. Specifically, we imagined a scenario in which an event, perhaps a merger, creates an initially high accretion rate that decreases over time. We suggested that Fe II absorption characterizes the high-accretion-rate stage when the infrared-luminous galaxy is shrugging off its cloak of dust and gas in a massive, thick outflow to become an ordinary quasar. The intermediate-accretion-rate stage produces an outflow that is no longer optically thick enough to include Fe^+ ions, keeping in mind that they are not found in the H II region of a photoionized gas, but rather at a larger depth, in the partially ionized zone. Finally, the Fe^+ absorption appears again when the quasar is running out of fuel (the low-accretion-rate branch). Specifically, we suggested that, among the FeLoBAL quasars with low accretion rates and outflows located close to the central engine, we are seeing absorption from Fe^+ present in the remnants of the failing torus.

While our speculative scenario involves the properties of the torus in general, it is worth noting that the data in hand cannot constrain torus models, as it is limited to the near-infrared band and only measures the hot dust emission likely from graphite grains at the very inner edge of the torus. Sophisticated torus models show that the hot dust emission can be at least partially decoupled from the thermal torus emission. For example, Stalevski et al. (2012) present 3D radiative transfer models of a clumpy two-phase torus. Their models reveal that the hot dust component may not be observed under various conditions. For example, the hot dust emission may not be observed from large angles from the normal, principally due to self absorption (their Figure 4); however, we do not believe this explanation applies to our objects, becase they are all Type 1s. But they also found weak hot dust emission in the case of low-contrast parameter, where the contrast parameterizes the density ratio between their high- and low-density phases (their Figure 9). While our suggestions are bolstered by many studies, as described in Section 8.1, much more data, especially at mid-IR wavelengths, would be necessary to test modern torus models and our speculative scenario in these objects.

Whether or not our speculative scenario has merit, there is no doubt that these four papers have a substantial impact on our understanding of FeLoBAL quasars. For example, the global covering fraction Ω, the fraction of 4π sterradians that includes outflow, is generally estimated based on the fraction of objects in a sample. This type of computation requires that the absorbed objects—in this case, the FeLoBALQs—differ from the unabsorbed ones *only* in their line-of-sight viewing angle. We have clearly shown that this assumption is violated among

the FeLoBAL quasars, implying that other methods are needed to estimate the global covering fraction. For example, if the absorption lines are narrow, then a comparison between observed emission lines and those predicted from the absorbing gas could give an estimate of the global covering fraction. Even then, this method might only give an upper limit if other sources of the line emission, i.e., from gas not associated with the outflow, are present in the quasar.

This sequence of papers has revealed how primitive, phenomenological, and incomplete some of our ideas about the quasar phenomenon are. It is startling that we could discover a new branch of the BAL outflow phenomenon using traditional analysis of archival ground-based spectroscopic data, given the maturity of the field of study. These papers exemplify the power of *SimBAL* analysis. The forward modeling semi-empirical approach allows us to directly constrain the physical parameters of the outflow as a function of velocity in the most complicated spectra. The relative ease of use allows us to compile detailed results from moderate-sized samples, which means that we can not only look for trends, but also place our analysis on a statistical footing.

At the same time, it is worth remembering that the quasar phenomenon is stochastic rather than deterministic. The stochasticity of the quasar phenomenon was discussed in the context of Type 2 AGN by Elitzur & Netzer (2016; see also Elitzur 2012). They argued that the luminosity cutoff consistent with the presence of a broad-line region depends on the black hole mass, but that the proportionality coefficient is not a single value and instead has a range of values due to factors that are not or cannot be modeled. Thus, it is certain that objects that do not conform to the scenario presented here can be found. While the cutoff for different accretion states in X-ray binaries may be well constrained (e.g., the $\dot{m}_{\rm crit} = \dot{M}/\dot{M}_{\rm Edd} = 0.01$–$0.02$ for the transition from hard to soft state), it seems reasonable that the different physics of accretion onto a million or billion times larger black hole would shift this value. A significant factor may be the fact that the accretion disk around a large black hole should emit in the UV where there is plenty of atomic opacity. This idea has been investigated by Jiang et al. (2016), who found that a modeled accretion disk that included atomic transitions, in particular the iron opacity that is also important in stellar winds, was more stable than one without atomic transitions.

Moving forward, we have embarked on an analysis of higher-redshift ($1.3 < z < 3$) FeLoBALQs; preliminary results have been presented in Voelker et al. (2021). Because of the flux-limited nature of SDSS, the higher-redshift objects are more luminous. More luminous objects are known to have faster outflows (e.g., Laor & Brandt 2002; Ganguly et al. 2007), and we have already found evidence for a higher incidence of energetic outflows among these more luminous objects. An interesting question is whether we will find many $E1 < 0$ FeLoBALQs, and in particular, the objects with loitering outflows. In the sample presented here, we found that about half of the objects have $E1 < 0$. Low-accretion-rate objects are predicted to fall out of flux-limited samples at higher redshifts (Jester et al. 2005), so we expect to find fewer of them. On the other hand, the loitering outflow objects have very characteristic FeLoBAL absorption spectra, and it may be that we can use those spectra to predict which objects should have low accretion rates. If we can find such objects at higher redshifts, we may find very massive black holes and possibly be able to place constraints on the scaling of the critical accretion rate $\dot{m}_{\rm crit}$ with black hole mass and/or luminosity.

Acknowledgments

K.M.L. acknowledges very useful conversations with Leah Morabito. Support for *SimBAL* development and analysis is provided by NSF Astronomy and Astrophysics grants No. 1518382, 2006771, and 2007023. This work was performed in part at Aspen Center for Physics, which is supported by National Science Foundation grant PHY-1607611. S.C.G. thanks the Natural Science and Engineering Research Council of Canada.

Long before the University of Oklahoma was established, the land on which the University now resides was the traditional home of the "Hasinais" Caddo Nation and "Kirikiris" Wichita & Affiliated Tribes. This land was also once part of the Muscogee Creek and Seminole nations.

We acknowledge this territory once also served as a hunting ground, trade exchange point, and migration route for the Apache, Comanche, Kiowa, and Osage nations. Today, 39 federally recognized Tribal nations dwell in what is now the State of Oklahoma as a result of settler colonial policies designed to assimilate Indigenous peoples.

The University of Oklahoma recognizes the historical connection our university has with its Indigenous community. We acknowledge, honor, and respect the diverse Indigenous peoples connected to this land. We fully recognize, support, and advocate for the sovereign rights of all of Oklahoma's 39 tribal nations.

This acknowledgment is aligned with our university's core value of creating a diverse and inclusive community. It is our institutional responsibility to recognize and acknowledge the people, culture, and history that make up our entire OU Community.

Funding for the SDSS and SDSS-II has been provided by the Alfred P. Sloan Foundation, the Participating Institutions, the National Science Foundation, the U.S. Department of Energy, the National Aeronautics and Space Administration, the Japanese Monbukagakusho, the Max Planck Society, and the Higher Education Funding Council for England. The SDSS website is http://www.sdss.org/.

The SDSS is managed by the Astrophysical Research Consortium for the Participating Institutions. The Participating Institutions are the American Museum of Natural History, Astrophysical Institute Potsdam, University of Basel, University of Cambridge, Case Western Reserve University, University of Chicago, Drexel University, Fermilab, the Institute for Advanced Study, the Japan Participation Group, Johns Hopkins University, the Joint Institute for Nuclear Astrophysics, the Kavli Institute for Particle Astrophysics and Cosmology, the Korean Scientist Group, the Chinese Academy of Sciences (LAMOST), Los Alamos National Laboratory, the Max-Planck-Institute for Astronomy (MPIA), the Max-Planck-Institute for Astrophysics (MPA), New Mexico State University, Ohio State University, University of Pittsburgh, University of Portsmouth, Princeton University, the United States Naval Observatory, and the University of Washington.

Funding for SDSS-III has been provided by the Alfred P. Sloan Foundation, the Participating Institutions, the National Science Foundation, and the U.S. Department of Energy Office of Science. The SDSS-III website is http://www.sdss3.org/.

SDSS-III is managed by the Astrophysical Research Consortium for the Participating Institutions of the SDSS-III Collaboration including the University of Arizona, the Brazilian Participation Group, Brookhaven National Laboratory, Carnegie Mellon University, University of Florida, the French Participation Group, the German Participation Group, Harvard University, the Instituto de Astrofisica de Canarias, the Michigan State/Notre Dame/JINA Participation Group, Johns Hopkins University, Lawrence Berkeley National Laboratory, Max Planck Institute for Astrophysics, Max Planck Institute for Extraterrestrial Physics, New Mexico State University, New York University, Ohio State University, Pennsylvania State University, University of Portsmouth, Princeton University, the Spanish Participation Group, University of Tokyo, University of Utah, Vanderbilt University, University of Virginia, University of Washington, and Yale University.

Facilities: IRTF (SpeX), Sloan, WISE, NEOWISE.

Software: Sherpa (Freeman et al. 2001), unTimelyCatalogExplorer (Kiwy 2022).

Appendix
Systematic Errors in the unTimely Catalog Photometry

The analysis was performed for each of the 30 FeLoBALQs and each of the 132 comparison objects. For each object, star candidates were identified from the AllWISE Source Catalog (TAP identifier `allwise_p3as_psd`) as follows. The potential star candidates were objects lying within circular region with a radius of 500″ around each quasar that also had W1 > 9, were less than 0.5 magnitudes dimmer than the corresponding object, and with color range $-0.2 < \mathrm{W1} - \mathrm{W2} < 0.2$. The time-series data were downloaded from the unTimely Catalog using the `unTimely_Catalog_explorer` (Kiwy 2022) using a box size of 1000″. All star candidates were required to have both W1 and W2 lightcurves.

The stars were chosen from the star candidates by requiring that the magnitude of the star lie within a range of the magnitude of the object. Because there are far more faint stars than bright ones, the range depended on the magnitude as $\Delta M = 0.7 - 0.125(W1_{\mathrm{object}} - 12.5)$. In addition, only lightcurves with 10 or more points were considered. The variance in the magnitude was computed for each star candidate. The mean of the catalog-obtained error squared was also collected. Figure 19 shows the relationship between these values for each star. There were 3293 W1 comparison stars and 661 W2 comparison stars. The values are different because quasars are relatively brighter in W2 compared with W1, and there is a lower density of brighter stars in the sky. The observed variance was found to be larger than the mean error squared, with the discrepancy being larger for the brighter objects. The origin of this discrepancy is not known. For each object, the median of the variance and the error squared is also plotted. Because of the outliers with unknown origin seen in the plot, the median was deemed more representative than the mean. These values are also shown in the plot.

As discussed in Section 4.3, the principal metric used for the variability was the excess variance, which is the difference between the variance of the object and the contribution due to noise in the data. We determined the contribution due to the noise in the data from the distribution of all of the stars shown in Figure 19. In bins of magnitude, the median, 16%, and 84% values of the distribution were computed. The results are seen in Figure 19. For each object, the variance due to noise was interpolated from the median relationship using the mean magnitude of the object. The uncertainties used in computing the excess variance in Section 4.3 were taken to be the 1σ bounds shown.

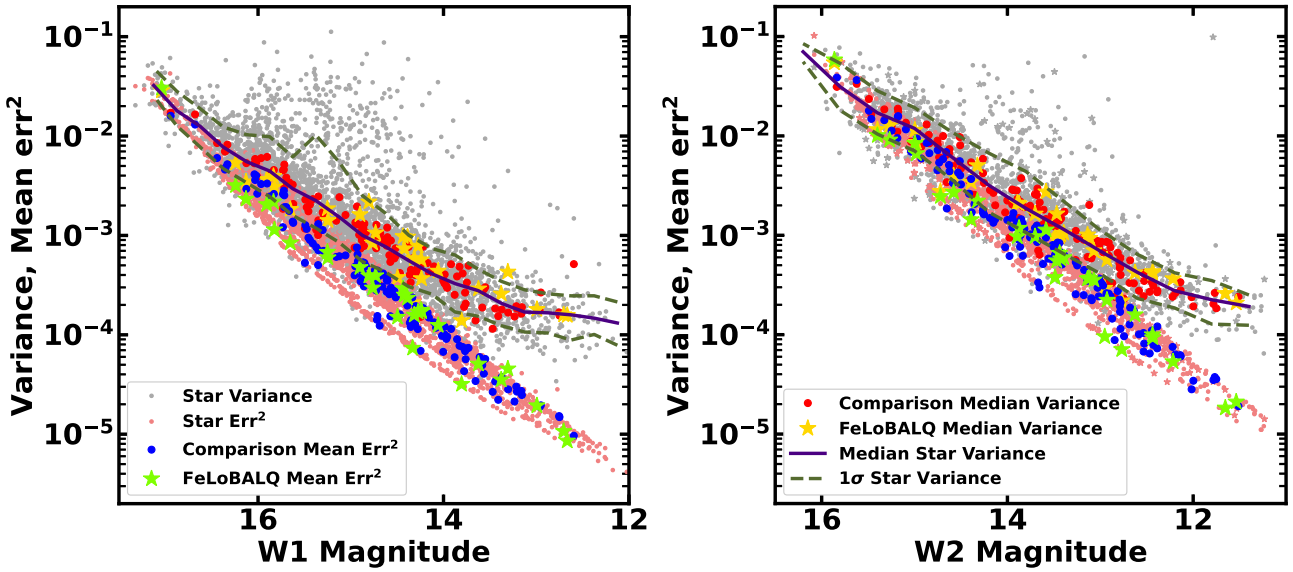

Figure 19. A comparison of the stellar lightcurve variance and the mean catalog error squared for the star candidates for both the W1 and W2 filters; legends apply to both panels. Most stars do not vary significantly. However, we found that the measured lightcurve variance (gray) is larger than the statistical error squared (pink), especially at lower magnitudes. We interpreted this as evidence for a systematic underestimation of the statistical errors. We defined a modified error as a function of magnitude based on the observed median (black line) and 16% and 84% cumulative distribution values (dashed gray lines).

ORCID iDs

Karen M. Leighly https://orcid.org/0000-0002-3809-0051
Hyunseop Choi (최현섭) https://orcid.org/0000-0002-3173-1098
Michael Eracleous https://orcid.org/0000-0002-3719-940X
Donald M. Terndrup https://orcid.org/0000-0002-0431-1645
Sarah C. Gallagher https://orcid.org/0000-0001-6217-8101
Gordon T. Richards https://orcid.org/0000-0002-1061-1804

References

Abramowicz, M. A., & Fragile, P. C. 2013, LRR, 16, 1
Aoki, K., Oyabu, S., Dunn, J. P., et al. 2011, PASJ, 63, 457
Arav, N., Brotherton, M. S., Becker, R. H., et al. 2001, ApJ, 546, 140
Arav, N., Moe, M., Costantini, E., et al. 2008, ApJ, 681, 954
Barr, P., & Mushotzky, R. F. 1986, Natur, 320, 421
Bautista, M. A., Dunn, J. P., Arav, N., et al. 2010, ApJ, 713, 25
Becker, R. H., Gregg, M. D., Hook, I. M., et al. 1997, ApJL, 479, L93
Bianchi, S., Antonucci, R., Capetti, A., et al. 2019, MNRAS, 488, L1
Blandford, R. D., & Payne, D. G. 1982, MNRAS, 199, 883
Blanton, M. R., Bershady, M. A., Abolfathi, B., et al. 2017, AJ, 154, 28
Bon, E., Popović, L. Č., Gavrilović, N., La Mura, G., & Mediavilla, E. 2009, MNRAS, 400, 924
Boroson, T. A. 2002, ApJ, 565, 78
Boroson, T. A., & Green, R. F. 1992, ApJS, 80, 109
Boroson, T. A., Meyers, K. A., Morris, S. L., & Persson, S. E. 1991, ApJL, 370, L19
Brotherton, M. S., Wills, B. J., Francis, P. J., & Steidel, C. C. 1994, ApJ, 430, 495
Calistro Rivera, G., Alexander, D. M., Rosario, D. J., et al. 2021, A&A, 649, A102
Capellupo, D. M., Netzer, H., Lira, P., Trakhtenbrot, B., & Mejía-Restrepo, J. 2015, MNRAS, 446, 3427
Caplar, N., Lilly, S. J., & Trakhtenbrot, B. 2017, ApJ, 834, 111
Cardelli, J. A., Clayton, G. C., & Mathis, J. S. 1988, ApJL, 329, L33
Chen, K., & Halpern, J. P. 1989, ApJ, 344, 115
Chen, K., Halpern, J. P., & Filippenko, A. V. 1989, ApJ, 339, 742
Choi, H., Leighly, K. M., Dabbieri, C., et al. 2022a, ApJ, 936, 110
Choi, H., Leighly, K. M., Terndrup, D. M., Gallagher, S. C., & Richards, G. T. 2020, ApJ, 891, 53
Choi, H., Leighly, K. M., Terndrup, D. M., et al. 2022b, ApJ, 937, 74
Constantin, A., Shields, J. C., Ho, L. C., et al. 2015, ApJ, 814, 149
Cushing, M. C., Vacca, W. D., & Rayner, J. T. 2004, PASP, 116, 362
Dabbieri, C., Leighly, K., & Richards, G. 2020, AAS Meeting Abstracts, 236, 238.03
Dai, X., Shankar, F., & Sivakoff, G. R. 2008, ApJ, 672, 108
Dai, X., Shankar, F., & Sivakoff, G. R. 2012, ApJ, 757, 180
Davis, S. W., & Laor, A. 2011, ApJ, 728, 98
Davis, S. W., Woo, J.-H., & Blaes, O. M. 2007, ApJ, 668, 682
De Cicco, D., Bauer, F. E., Paolillo, M., et al. 2022, A&A, 664, A117
de Kool, M., Arav, N., Becker, R. H., et al. 2001, ApJ, 548, 609
de Kool, M., Becker, R. H., Arav, N., Gregg, M. D., & White, R. L. 2002a, ApJ, 570, 514
de Kool, M., Becker, R. H., Gregg, M. D., White, R. L., & Arav, N. 2002b, ApJ, 567, 58
DiPompeo, M. A., Brotherton, M. S., & De Breuck, C. 2013, MNRAS, 428, 1565
DiPompeo, M. A., Hickox, R. C., Carroll, C. M., et al. 2018, ApJ, 856, 76
Dumont, A. M., & Collin-Souffrin, S. 1990, A&A, 229, 313
Dunn, J. P., Bautista, M., Arav, N., et al. 2010, ApJ, 709, 611
Elitzur, M. 2008, NewAR, 52, 274
Elitzur, M. 2012, ApJL, 747, L33
Elitzur, M., & Ho, L. C. 2009, ApJL, 701, L91
Elitzur, M., & Netzer, H. 2016, MNRAS, 459, 585
Elitzur, M., & Shlosman, I. 2006, ApJL, 648, L101
Elvis, M., Marengo, M., & Karovska, M. 2002, ApJL, 567, L107
Eracleous, M. 2002, in ASP Conf. Ser. 255, Mass Outflow in Active Galactic Nuclei: New Perspectives, ed. D. M. Crenshaw, S. B. Kraemer, & I. M. George (San Francisco, CA: ASP), 131
Eracleous, M., Halpern, J. P., & Charlton, J. C. 2003, ApJ, 582, 633
Everett, J., Königl, A., & Arav, N. 2002, ApJ, 569, 671
Faucher-Giguère, C.-A., Quataert, E., & Murray, N. 2012, MNRAS, 420, 1347
Francis, P. J., Hewett, P. C., Foltz, C. B., et al. 1991, ApJ, 373, 465
Freeman, P., Doe, S., & Siemiginowska, A. 2001, Proc. SPIE, 4477, 76
Fynbo, J. P. U., Krogager, J. K., Venemans, B., et al. 2013, ApJS, 204, 6
Gallagher, S. C., Everett, J. E., Abado, M. M., & Keating, S. K. 2015, MNRAS, 451, 2991
Gallagher, S. C., Richards, G. T., Lacy, M., et al. 2007, ApJ, 661, 30
Gallastegui-Aizpun, U., & Sarajedini, V. L. 2014, MNRAS, 444, 3078
Ganguly, R., Brotherton, M. S., Cales, S., et al. 2007, ApJ, 665, 990
Gibson, R. R., Jiang, L., Brandt, W. N., et al. 2009, ApJ, 692, 758
Glikman, E. 2017, RNAAS, 1, 48
Glikman, E., Gregg, M. D., Lacy, M., et al. 2004, ApJ, 607, 60
Glikman, E., Helfand, D. J., & White, R. L. 2006, ApJ, 640, 579
Glikman, E., Simmons, B., Mailly, M., et al. 2015, ApJ, 806, 218
Glikman, E., Urrutia, T., Lacy, M., et al. 2012, ApJ, 757, 51
González-Martín, O., Masegosa, J., Hernán-Caballero, A., et al. 2017, ApJ, 841, 37
Green, A. R., McHardy, I. M., & Lehto, H. J. 1993, MNRAS, 265, 664
Green, P. J., Aldcroft, T. L., Mathur, S., Wilkes, B. J., & Elvis, M. 2001, ApJ, 558, 109
Green, R. F., Schmidt, M., & Liebert, J. 1986, ApJS, 61, 305
Hall, P. B., Anderson, S. F., Strauss, M. A., et al. 2002, ApJS, 141, 267
Halpern, J. P., Eracleous, M., Filippenko, A. V., & Chen, K. 1996, ApJ, 464, 704
Hamann, F., Tripp, T. M., Rupke, D., & Veilleux, S. 2019, MNRAS, 487, 5041
Hewett, P. C., & Foltz, C. B. 2003, AJ, 125, 1784
Hopkins, P. F., Hernquist, L., Martini, P., et al. 2005, ApJL, 625, L71
Hopkins, P. F., Hickox, R., Quataert, E., & Hernquist, L. 2009, MNRAS, 398, 333
Izumi, T., Kohno, K., Fathi, K., et al. 2017, ApJL, 845, L5
Jester, S., Schneider, D. P., Richards, G. T., et al. 2005, AJ, 130, 873
Jiang, P., Zhou, H., Ji, T., et al. 2013, AJ, 145, 157
Jiang, Y.-F., Davis, S. W., & Stone, J. M. 2016, ApJ, 827, 10
Kelly, B. C., Bechtold, J., & Siemiginowska, A. 2009, ApJ, 698, 895
Kiwy, F., 2022 unTimely_Catalog_explorer: A Search and Visualization Tool for the unTimely Catalog, Astrophysics Source Code Library, ascl:2211.005
Klindt, L., Alexander, D. M., Rosario, D. J., Lusso, E., & Fotopoulou, S. 2019, MNRAS, 488, 3109
Knigge, C., Scaringi, S., Goad, M. R., & Cottis, C. E. 2008, MNRAS, 386, 1426
Kokubo, M., Morokuma, T., Minezaki, T., et al. 2014, ApJ, 783, 46
Konigl, A., & Kartje, J. F. 1994, ApJ, 434, 446
Koratkar, A., & Blaes, O. 1999, PASP, 111, 1
Korista, K. T., Bautista, M. A., Arav, N., et al. 2008, ApJ, 688, 108
Krawczyk, C. M., Richards, G. T., Gallagher, S. C., et al. 2015, AJ, 149, 203
Krawczyk, C. M., Richards, G. T., Mehta, S. S., et al. 2013, ApJS, 206, 4
Krogager, J. K., Fynbo, J. P. U., Heintz, K. E., et al. 2016, ApJ, 832, 49
Krogager, J. K., Geier, S., Fynbo, J. P. U., et al. 2015, ApJS, 217, 5
Krogager, J. K., Leighly, K. M., Fynbo, J. P. U., et al. 2023, Msngr, 190, 38
La Mura, G., Di Mille, F., Ciroi, S., Popović, L. Č, & Rafanelli, P. 2009, ApJ, 693, 1437
Laor, A., & Brandt, W. N. 2002, ApJ, 569, 641
Laurenti, M., Vagnetti, F., Middei, R., & Paolillo, M. 2020, MNRAS, 499, 6053
Lawrence, A., & Papadakis, I. 1993, ApJL, 414, L85
Lawrence, A., Warren, S. J., Almaini, O., et al. 2007, MNRAS, 379, 1599
Lazarova, M. S., Canalizo, G., Lacy, M., et al. 2023, ApJ, 949, 69
Leighly, K. M. 1999, ApJS, 125, 297
Leighly, K. M., Choi, H., DeFrancesco, C., et al. 2022, ApJ, 935, 92
Leighly, K. M., Hamann, F., Casebeer, D. A., & Grupe, D. 2009, ApJ, 701, 176
Leighly, K. M., Kay, L. E., Wills, B. J., Wills, D., & Grupe, D. 1997, ApJL, 489, L137
Leighly, K. M., & Moore, J. R. 2006, ApJ, 644, 748
Leighly, K. M., Terndrup, D. M., Gallagher, S. C., Richards, G. T., & Dietrich, M. 2018, ApJ, 866, 7
Leighly, K. M., Terndrup, D. M., Lucy, A. B., et al. 2019, ApJ, 879, 27
López-Navas, E., Arévalo, P., Bernal, S., et al. 2023, MNRAS, 518, 1531
Low, F. J., Cutri, R. M., Kleinmann, S. G., & Huchra, J. P. 1989, ApJL, 340, L1
Lucy, A. B., Knigge, C., & Sokoloski, J. L. 2018, MNRAS, 478, 568
Lucy, A. B., Leighly, K. M., Terndrup, D. M., Dietrich, M., & Gallagher, S. C. 2014, ApJ, 783, 58
Lyu, J., Rieke, G. H., & Shi, Y. 2017, ApJ, 835, 257
MacLeod, C. L., & Ivezić, Ž. 2010, ApJ, 721, 1014
Martin, D. C., Fanson, J., Schiminovich, D., et al. 2005, ApJL, 619, L1
McHardy, I. 1985, SSRv, 40, 559
Meisner, A. M., Caselden, D., Schlafly, E. F., & Kiwy, F. 2023, AJ, 165, 36

Meusinger, H., Schalldach, P., Mirhosseini, A., & Pertermann, F. 2016, A&A, 587, A83
Mitchell, J. A. J., Done, C., Ward, M. J., et al. 2023, MNRAS, 524, 1796
Moe, M., Arav, N., Bautista, M. A., & Korista, K. T. 2009, ApJ, 706, 525
Morabito, L. K., Dai, X., Leighly, K. M., Sivakoff, G. R., & Shankar, F. 2011, ApJ, 737, 46
Nandra, K., George, I. M., Mushotzky, R. F., Turner, T. J., & Yaqoob, T. 1997, ApJ, 476, 70
Pâris, I., Petitjean, P., Aubourg, E. ´, et al. 2018, A&A, 613, A51
Pâris, I., Petitjean, P., Ross, N. P., et al. 2017, A&A, 597, A79
Polletta, M., Tajer, M., Maraschi, L., et al. 2007, ApJ, 663, 81
Rayner, J. T., Toomey, D. W., Onaka, P. M., et al. 2003, PASP, 115, 362
Reichard, T. A., Richards, G. T., Hall, P. B., et al. 2003, AJ, 126, 2594
Ricci, C., Trakhtenbrot, B., Koss, M. J., et al. 2017, Natur, 549, 488
Richards, G. T., Lacy, M., Storrie-Lombardi, L. J., et al. 2006, ApJS, 166, 470
Sabra, B. M., Shields, J. C., Ho, L. C., Barth, A. J., & Filippenko, A. V. 2003, ApJ, 584, 164
Sanders, D. B., Soifer, B. T., Elias, J. H., Neugebauer, G., & Matthews, K. 1988a, ApJL, 328, L35
Sanders, D. B., Soifer, B. T., Elias, J. H., et al. 1988b, ApJ, 325, 74
Schlafly, E. F., & Finkbeiner, D. P. 2011, ApJ, 737, 103
Schulze, A., Misawa, T., Zuo, W., & Wu, X.-B. 2018, ApJ, 853, 167
Schulze, A., Schramm, M., Zuo, W., et al. 2017, ApJ, 848, 104
Shen, Y., & Ho, L. C. 2014, Natur, 513, 210
Shi, X.-H., Jiang, P., Wang, H.-Y., et al. 2016, ApJ, 829, 96
Shields, J. C., Sabra, B. M., Ho, L. C., Barth, A. J., & Filippenko, A. V. 2002, in ASP Conf Ser. 255, Mass Outflow in Active Galactic Nuclei: New Perspectives, ed. D. M. Crenshaw, S. B. Kraemer, & I. M. George (San Francisco, CA: ASP), 105
Simm, T., Salvato, M., Saglia, R., et al. 2016, A&A, 585, A129
Skrutskie, M. F., Cutri, R. M., Stiening, R., et al. 2006, AJ, 131, 1163
Slone, O., & Netzer, H. 2012, MNRAS, 426, 656
Stalevski, M., Fritz, J., Baes, M., Nakos, T., & Popović, L. 2012, MNRAS, 420, 2756
Stern, D., Assef, R. J., Benford, D. J., et al. 2012, ApJ, 753, 30
Stirpe, G. M. 1991, A&A, 247, 3
Storchi-Bergmann, T., Schimoia, J. S., Peterson, B. M., et al. 2017, ApJ, 835, 236
Suberlak, K. L., & Ivezić, Ž. 2021, ApJ, 907, 96
Sun, M., Xue, Y., Wang, J., Cai, Z., & Guo, H. 2018, ApJ, 866, 74
Temple, M. J., Banerji, M., Hewett, P. C., Rankine, A. L., & Richards, G. T. 2021, MNRAS, 501, 3061
Tolea, A., Krolik, J. H., & Tsvetanov, Z. 2002, ApJL, 578, L31
Trump, J. R., Hall, P. B., Reichard, T. A., et al. 2006, ApJS, 165, 1
Trump, J. R., Impey, C. D., Kelly, B. C., et al. 2011, ApJ, 733, 60
Turnshek, D. A., Monier, E. M., Sirola, C. J., & Espey, B. R. 1997, ApJ, 476, 40
Urrutia, T., Becker, R. H., White, R. L., et al. 2009, ApJ, 698, 1095
Urrutia, T., Lacy, M., Spoon, H., et al. 2012, ApJ, 757, 125
Vacca, W. D., Cushing, M. C., & Rayner, J. T. 2003, PASP, 115, 389
van der Wolk, G., Barthel, P. D., Peletier, R. F., & Pel, J. W. 2010, A&A, 511, A64
Vanden Berk, D. E., Shen, J., Yip, C.-W., et al. 2006, AJ, 131, 84
Vanden Berk, D. E., Wilhite, B. C., Kron, R. G., et al. 2004, ApJ, 601, 692
Voelker, J., Choi, H., Leighly, K., DeFrancesco, C., & Dabbieri, C. 2021, AAS Meeting Abstracts, 53, 337.10
Whysong, D., & Antonucci, R. 2004, ApJ, 602, 116
Wilhite, B. C., Brunner, R. J., Grier, C. J., Schneider, D. P., & vanden Berk, D. E. 2008, MNRAS, 383, 1232
Wills, B. J., Wills, D., Evans, N. J., II, et al. 1992, ApJ, 400, 96
Wright, E. L., Eisenhardt, P. R. M., Mainzer, A. K., et al. 2010, AJ, 140, 1868
Yu, W., Richards, G. T., Vogeley, M. S., Moreno, J., & Graham, M. J. 2022, ApJ, 936, 132
Zhang, S., Wang, H., Wang, T., et al. 2014, ApJ, 786, 42
Zuo, W., Wu, X.-B., Liu, Y.-Q., & Jiao, C.-L. 2012, ApJ, 758, 104